LITHOS 482–483 (2024) 107703

Contents lists available at ScienceDirect

LITHOS

journal homepage: www.elsevier.com/locate/lithos

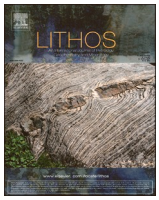

Petrogenesis of the pyroxenitic Moho transition zone in the Zedong ophiolite, Southeastern Tibet

Zhen-Yu Zhang [a], Chuan-Zhou Liu [a,b,c,*], Yan Liang [d], Liang-Liang Zhang [e], Chang Zhang [a], Tong Liu [a], Bo-Da Liu [a], Wei-Qi Zhang [a], Yin-Zheng Lin [a,c], Wen-Bin Ji [f]

[a] State Key Laboratory of Lithospheric Evolution, Institute of Geology and Geophysics, Chinese Academy of Sciences, Beijing 100029, China
[b] Laoshan Laboratory, Qingdao 266273, China
[c] College of Earth and Planetary Sciences, University of Chinese Academy of Sciences, Beijing 100049, China
[d] Department of Earth, Environmental and Planetary Sciences, Brown University, Providence, RI 02912, USA
[e] State Key Laboratory of Geological Processes and Mineral Resources, and Institute of Earth Sciences, China University of Geosciences, Beijing 100083, China
[f] Department of Geology, Northwest University, Xi'an, Shaanxi Province 710069, China

ARTICLE INFO

Keywords:
Zedong ophiolite
Moho transition zone
Pyroxenite
Hydrous differentiation
Crystal fractionation
Nd-Hf isotopes

ABSTRACT

Understanding the petrological and geochemical processes shaping the Moho transition zone (MTZ) is crucial for advancing our knowledge of thermal and chemical exchanges between the oceanic crust and the residual upper mantle. In this study, we systematically investigate the MTZ outcropped within the Zedong ophiolite, located in the eastern part of the Yarlung-Tsangpo Suture Zone (YTSZ), with the aim of at reconstructing the magmatic processes responsible for generating the petrological Moho. The Zedong MTZ comprises a sequence of dunite, wehrlite, pyroxenite, and gabbro, with frequent occurrences of clinopyroxene-rich lithologies. Cyclicity within the MTZ sequences is characterized by the recurrence of olivine-rich intervals and the presence of zig-zag patterns in both major and trace elements of clinopyroxenes. Zircon U—Pb dating on the Zedong gabbros supports the coeval formation of the Zedong ophiolite with other YTSZ ophiolites. Clinopyroxene in the Zedong MTZ follows a differentiation sequence characterized by an increase in contents of Al_2O_3 and TiO_2, coupled with a decrease in Mg#. This differentiation sequence along with frequent occurrences of amphibole suggest the evolution of a primitive hydrous melt depleted in Al_2O_3, TiO_2, and Na_2O. The depleted Nd—Hf isotopes and rare earth element patterns of the MTZ rocks indicate that their parental magmas originated from fluid-enhanced re-melting of a previously depleted mantle. Additionally, we proposed that the initiation of a new subduction zone results in the re-melting of the mantle peridotite, leading to the formation of primitive hydrous basaltic melts. The variable lithologies observed in the Zedong MTZ arise from fractional crystallization and repeated replenishment of hydrous melts.

1. Introduction

The Moho Transition Zone (MTZ) serves as a critical interface between the upwelling mantle and accreting crust. Within this zone, peridotites are associated with mafic and ultramafic rocks, forming the harzburgite-dunite-gabbro sequence, with varying proportions of wehrlite and pyroxenite (Boudier and Nicolas, 1995), as observed at the mid-Atlantic ridge (e.g., Drouin et al., 2009; Kelemen et al., 2007; Takazawa et al., 2007), the East Pacific Rise (e.g., Arai and Takemoto, 2007; Dick and Natland, 1996; Girardeau and Francheteau, 1993), the Parece Vela back-arc basin (Sanfilippo et al., 2013), and in numerous ophiolites (e.g., Akizawa and Arai, 2009; Akizawa et al., 2012; Batanova et al., 2005; Ceuleneer and Le Sueur, 2008; Koga et al., 2001; Koepke et al., 2009; Sano and Kimura, 2007). The occurrence and abundance of the MTZ lithologies vary significantly on both regional and local scales (e.g., Ceuleneer and Le Sueur, 2008; Dick et al., 2010; Jousselin et al., 2021; Kelemen et al., 2007; Rospabé et al., 2019; Tamura et al., 2008).

Although the origin of the MTZ has not been fully resolved and is likely case-dependent, it generally involves melts extracted from the mantle aggregate, circulating, reacting with peridotite, and partially crystallizing, before feeding the overlying crust (e.g., Abily and Ceuleneer, 2013; Boudier and Nicolas, 1995; Jousselin et al., 2021; Karson

* Corresponding author at: State Key Laboratory of Lithospheric Evolution, Institute of Geology and Geophysics, Chinese Academy of Sciences, Beijing 100029, China.
E-mail address: chzliu@mail.iggcas.ac.cn (C.-Z. Liu).

https://doi.org/10.1016/j.lithos.2024.107703
Received 28 March 2024; Received in revised form 18 June 2024; Accepted 18 June 2024
Available online 21 June 2024

et al., 1984; Nicolle et al., 2016). Among the diverse MTZ lithologies, the most enigmatic rocks are clinopyroxene-rich wehrlite and pyroxenite, which are primarily composed of olivine and clinopyroxene. They typically form at low crystallization pressures and often exhibit a characteristic cumulate texture, suggesting that these rocks were formed by accumulation of olivine and clinopyroxene in a shallow crustal magma chamber. Given that plagioclase is stable in mid ocean ridge systems at shallow pressures (e.g., Grove et al., 1992; Villiger et al., 2007), the questions arise which mechanism is responsible for the suppression of plagioclase crystallization. Two major processes have been proposed for the formation of wehrlite and pyroxenite in the MTZ: (1) The presence of water in basaltic systems prevented the crystallization of plagioclase. This model could account for many wehrlites and clinopyroxenites occurring in the crust of subduction zone-related ophiolites, where a hydrous melt is derived from subduction processes (e.g., Bağci et al., 2005; Batanova et al., 2005; Ceuleneer and Le Sueur, 2008). (2) Melt-peridotite reaction between the anhydrous mid ocean ridge basalt (MORB) and peridotite, followed by subsequent cooling at low pressures, could also generate wehrlite and pyroxenite within the MTZ (e.g., Abily and Ceuleneer, 2013; Benn et al., 1988; Girardeau and Francheteau, 1993; Nicolle et al., 2016; Saper and Liang, 2014).

The present study focuses on the MTZ within the Zedong ophiolite, which is located on the at the eastern segment of the Yarlung-Tsangpo suture Zone (YTSZ). Previous studies have investigated the structural, petrological, and geochemical features of mantle peridotites and the mafic dikes intruding the mantle peridotites (e.g., Lai et al., 2015; Xiong et al., 2016, 2017). However, very little attention has been paid to the MTZ at the Zedong ophiolite. The Zedong MTZ are separated from ophiolitic sections of the mantle peridotites and mélanges by thrust faults, featuring a continuous section with thickness ranging from ~50 to 1000 m. Compared to the MTZ sequences from the Luobusa and Oman ophiolite, the Zedong MTZ appears to be partly dismembered, with notable absence of lower oceanic crust and thick dunite layers (e.g., Jousselin et al., 2021; Zhou et al., 2005). Here, we present, for the first time, a detailed petrological and geochemical study of dunite-wehrlite, pyroxenite, and gabbro within the Zedong MTZ, which enable us to systematically investigate the magmatic processes leading to the formation of the MTZ and the nature of their mantle source. We demonstrate that the Zedong MTZ originated through a process involving fractional crystallization and repeated replenishments of hydrous melts in an initial subduction zone at the beginning of the interoceanic thrusting.

2. Geological setting and sample description

2.1. Geological setting

The Yarlung-Tsangpo Suture Zone (YTSZ) demarcates the Indian plate to the south and the Eurasian plate to the north, along which the Yarlung-Tsangpo ophiolites (YTO) are discontinuously outcropped. The YTO represent remnants of the Neo-Tethyan oceanic lithosphere, which extends in an almost east-west orientation from the Ladakh region in the west to the Namche Barwa syntaxis in the east (Fig. 1a). Geologically, the YTO are sandwiched between the Tethyan Himalayan unit in the south, and the Luobusa conglomerate belt and the Xigaze forearc basin in the north (Fig. 1b). Two nearly W-E trending Cenozoic thrust systems, i.e., the S-dipping Renbu-Zedong Thrust system and the N-dipping Gangdese Thrust system, localize the YTSZ between the northern margin of the India plate and the Gangdese Arc lying on the Lhasa Block (e.g., Liang et al., 2011; Yin, 2000). Compared to the Penrose-type ophiolites, the YTO commonly have very thin sections of cumulus gabbros, with a thickness much <3 km (Girardeau et al., 1985; Liu et al., 2020a; Nicolas et al., 1981). Multiple gabbroic and diabasic dykes with ages of ~130–120 Ma crosscut both the mantle and crust sections (e.g., Liu et al., 2016; Zhang et al., 2016a; Zhang et al., 2016b; Zhang et al., 2023a). Mélanges comprising of amphibolites and garnet-amphibolites commonly occur underneath the mantle section of the YTO, with protolith U—Pb ages of 125–124 Ma and ^{40}Ar—^{39}Ar cooling ages of ~123

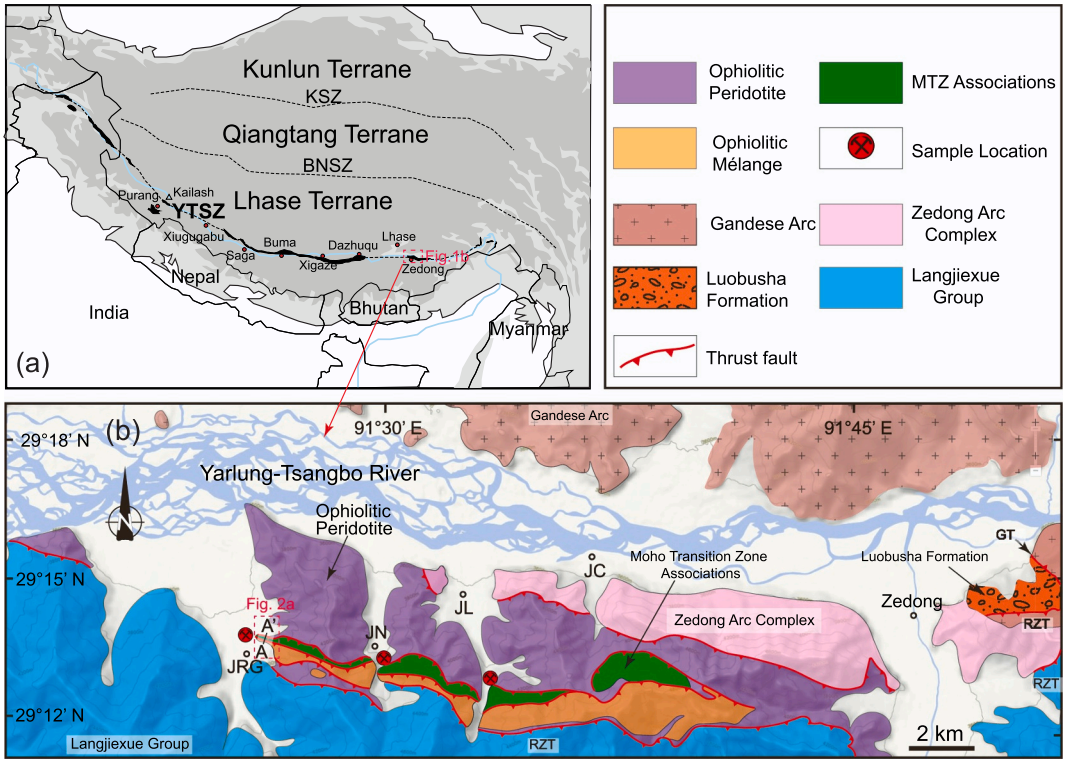

Fig. 1. (a) Sketch map of the Tibetan Plateau, modified after (Guilmette et al., 2009), illustrating the spatial distributions of key suture zones and tectonic units. KSZ: Kunlun suture zone, BNSZ Bangong-Nujiang suture zone, and YTSZ: Yarlung-Tsangpo suture zone. (b) Geological sketch map of the Zedong ophiolite, adapted from (Xiong et al., 2016), featuring three designated sample localities.

Ma (Guilmette et al., 2012; Zhang et al., 2019). The tectonic context of the YTO remains controversial, with three main hypotheses: (1) a Mid-Ocean Ridge (MOR; e.g., Li et al., 2022; Liu et al., 2014; Liu et al., 2022; Xiong et al., 2022; Zhou et al., 2023), (2) a Supra-Subduction Zone (SSZ) setting (e.g., Dai et al., 2013; Lian et al., 2016; Xiong et al., 2016, 2017; Yang et al., 2024), and (3) a multi-stage model where the YTO was initially generated in a MOR setting and subsequently modified in a SSZ (e.g., Hébert et al., 2012; Liu et al., 2010; Zhou et al., 2005).

2.2. Sample descriptions

The Zedong ophiolite is situated between the Triassic Langjiexue flysch in the south and the Jurassic Zedong arc complex (part of the Gangdese arc) in the north (Fig. 1b; Zhang et al., 2014). The Zedong ophiolitic massif is subdivided into three sub-units separated by thrusts, which, include the peridotite massif, the mélange with mafic blocks within serpentinites, and the MTZ containing predominantly clinopyroxenite with occasional layers of dunite, wehrlite, and gabbro (Fig. 2a). Within the clinopyroxenite section, coarse-grained clinopyroxenites (C-Cpxnite) occur as lenses within a fine-grained olivine-clinopyroxenite (F-Cpxnite) matrix (Fig. 2c and d). Magmatic layering is defined by variations in relative abundance and/or grain sizes (~2–15 mm) of the clinopyroxene, olivine, and plagioclase (Fig. 2). Foliations observed in the magmatic layers of various lithologies within the MTZ are nearly perpendicular to foliations of peridotites in the mantle section (Fig. 2c and e-g).

We sampled three subunits in the Moho Transition Zone within the Zedong ophiolite: the Jinlu (JL), Jieni (JN), and Jiaregang (JRG) within the Zedong ophiolite (Fig. 1b). The rock associations within the Zedong MTZ undergo severe serpentinization (Fig. 2 and Appendix 1). Specifically, nearly all olivines have undergone complete alteration to serpentine, while clinopyroxenes remain relatively fresh (Appendix 1). The pyroxenites, containing 59–98 vol% clinopyroxene, range from olivine clinopyroxenite to clinopyroxenite (Table S1). These pyroxenites can be categorized into two groups based on contrasting sizes of euhedral to subhedral clinopyroxene grains: C-Cpxnite, characterized by grains exceeding 5 mm in width, and F-Cpxnite, characterized by grains approximately 2–5 mm in width. Both F-Cpxnite and C-Cpxnite display polygonal, equigranular, and adcumulate textures (Fig. 3a). Small amounts of olivine-orthopyroxene-clinopyroxene matrix (< 1 mm in width) occur along grain boundaries of clinopyroxenes (Fig. 3b–d). It is worth noting the absence of plagioclase in the C-Cpxnite and F-Cpxnite sections. We selected three wehrlite samples (18JRG5–1, 23JRG1–2-1, and 23JRG1–2-2) for detail study. The textures of these three samples

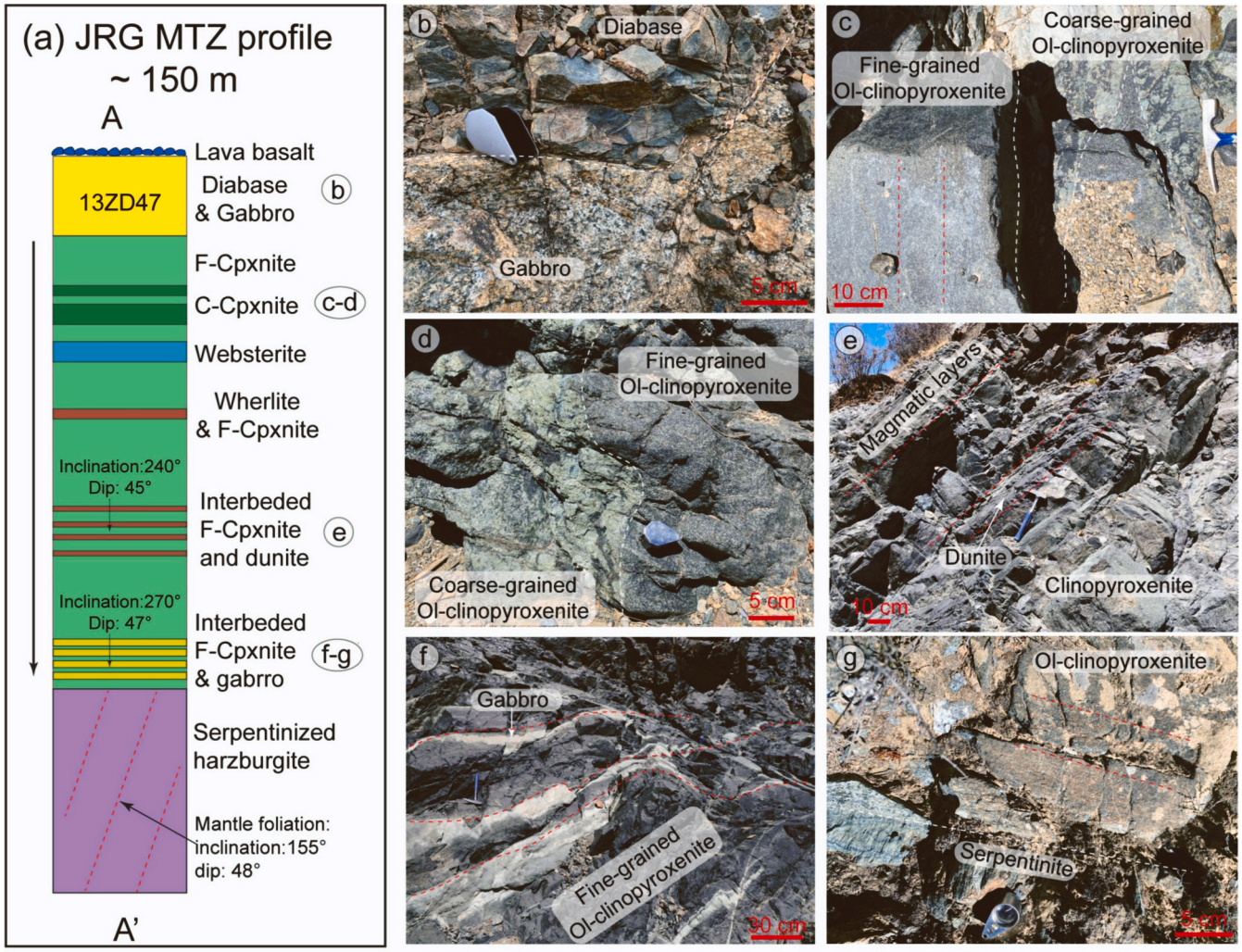

Fig. 2. (a) Schematic pseudostratigraphic diagram depicting the reconstructed lithospheric architecture along the Jiaregang profile (A-A') within the Zedong ophiolite. (b) Sharp contact between intruding diabase dike and the gabbroic host. (c-d) Coarse-grained olivine clinopyroxenite vein intruding into fine-grained clinopyroxenite. (e) Alternating layers of dunite (dark black) and clinopyroxenite (grey) with delineated interfaces (red lines). (f) Interbedded gabbros and fine-grained olivine clinopyroxenite. (g) Sharp contact between serpentine and clinopyroxenite. (For interpretation of the references to colour in this figure legend, the reader is referred to the web version of this article.)

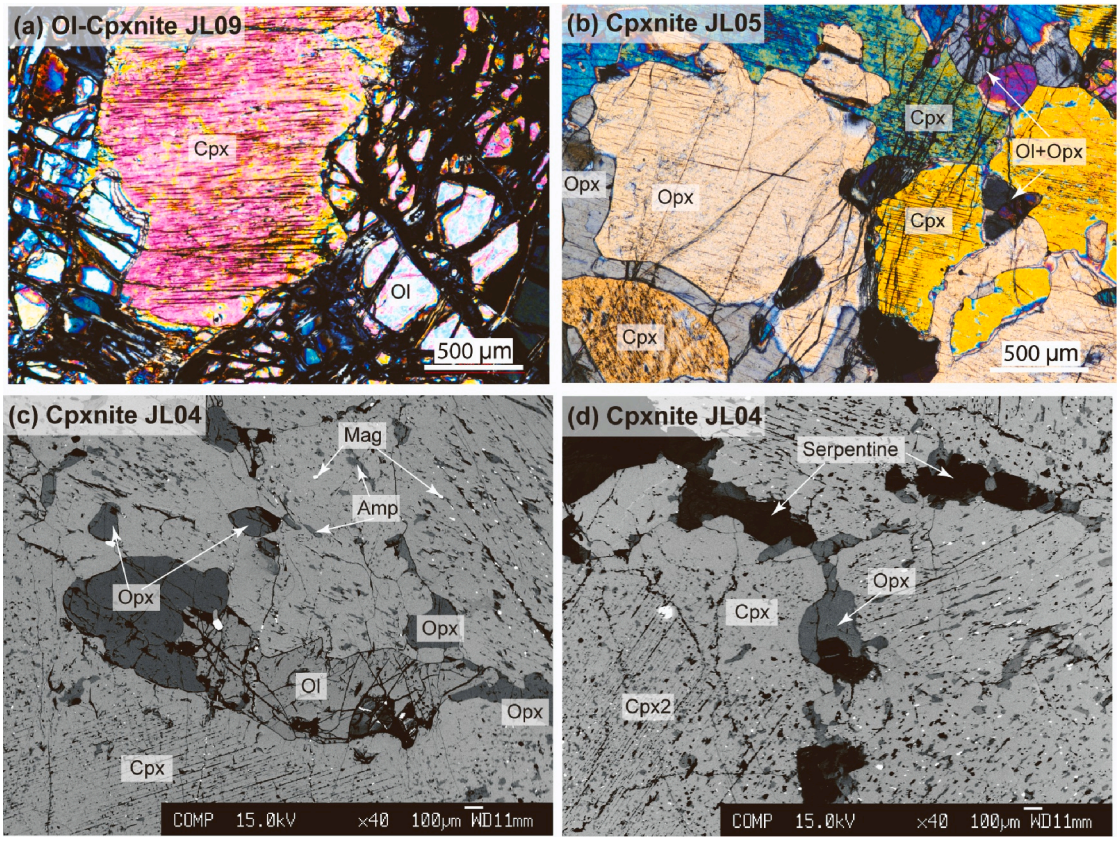

Fig. 3. Photomicrographs of (olivine-) clinopyroxenite samples from the Zedong ophiolite. (a) Co-crystallization of olivine and clinopyroxene in the coarse-grained olivine clinopyroxenite (18JL09). (b) Flame-like occurences of orthopyroxene and clinopyroxene in the interstitial regions of clinopyroxenite 18JL05. (c-d) Partially serpentinization of interstitial olivine and orthopyroxene within clinopyroxenite 18JL04, with an amphibole and magnetite mainly concentrated at the clinopyroxene margins or along orthopyroxene exsolution lamellae.

closely resemble those of F-Cpxnite, distinguished primarily by a higher modal abundance of olivine (Figs. S1.4 and S1.7 in Appendix 1, Table S1).

The websterite sample 18JRG04 was located in the upper part of the JRG MTZ (Fig. 2a), characterized by an equigranular texture consisting of 67 vol% clinopyroxene and 33 vol% orthopyroxene (Fig. S1.7 in Appendix 1). For completeness, we also selected three (olivine-) gabbros and one plagioclase-clinopyroxenite that are interbedded with olivine-clinopyroxenites (Fig. 2a). These three samples all display adcumulate textures with fine-grained clinopyroxene that are partly altered to amphibole. All of the olivine and plagioclase within these three samples are totally altered to serpentine and chlorite + prehnite, respectively (Appendix 1). Finally, the olivine gabbro 18JRG02 contains fine-grained clinopyroxene (39 vol%), completely altered plagioclase (29 vol%), and severely serpentinized olivine (31 vol%, Table S1 and Appendix 1).

3. Analytical methods

All measurements in this study were conducted at the Institute of Geology and Geophysics, Chinese Academy of Science, Beijing, China. Thin-section micro X-ray fluorescence mapping measurements were performed using a Bruker M4 Tornado PLUS spectrometer (Bruker Nano GmbH, Berlin, Germany). Bulk rock major and trace element concentrations were obtained using X-ray fluorescence spectroscopy and inductively coupled plasma mass spectrometry (ICP-MS), respectively. Mineral major element and trace element abundances were determined using a Cameca SX Five electron microprobe and a laser ablation inductively coupled plasma mass spectrometry (LA-ICP-MS), respectively. Neodymium and hafnium isotopic compositions were obtained using the isotope dilution method and subsequently measured using a Thermo Fisher Neptune plus multi-collector mass spectrometer. Detailed analytical procedures, precision, and accuracy of our measurements are provided in the online supplementary materials (Appendix 2 and Table S1–S6).

4. Results

4.1. Whole rock major and trace elements

Whole rock major and trace element abundances are listed in Table S2, which are consistent with their rock types and primarily reflect modal variations (Fig. 4a). Here we will highlight several key observations. The loss on ignition (LOI) fall within the range of 0.90 wt% to 4.72 wt%, primarily reflecting the degree of serpentinization in the samples. Thirteen (olivine-) clinopyroxenite and websterite samples display large variations in their Mg# [=100 × Mg/(Mg + Fe), all in molar fractions], ranging from 83 to 91 (Fig. 4a). These samples have notably low concentrations of Al_2O_3 (1.13–2.95 wt%), TiO_2 (0.06–0.33 wt%) and Na_2O (0.03–0.22 wt%) (Figs. 4b, c, and Table S2). Two gabbroic samples display distinct major element compositions, with Mg# values falling between 73 and 83, Al_2O_3 ranging from 8.72 to 19.92 wt%, and total alkali ($Na_2O + K_2O$) contents varying from 0.23 to 6.03 wt% (Figs. 4b, c, and Table S2).

In the primitive mantle normalized spider diagram, the Zedong pyroxenite and gabbro show consistently depleted patterns in light rare earth elements (LREE) and relatively flat patterns in middle to heavy REE (Fig. 5). Additionally, the Zedong MTZ samples demonstrate significant enrichments in large ion lithophile elements (LILE), such as Rb and Ba. Most of the samples show positive anomalies of Sr. The exception is the websterite (18JRG02) that displays a negative Sr anomaly.

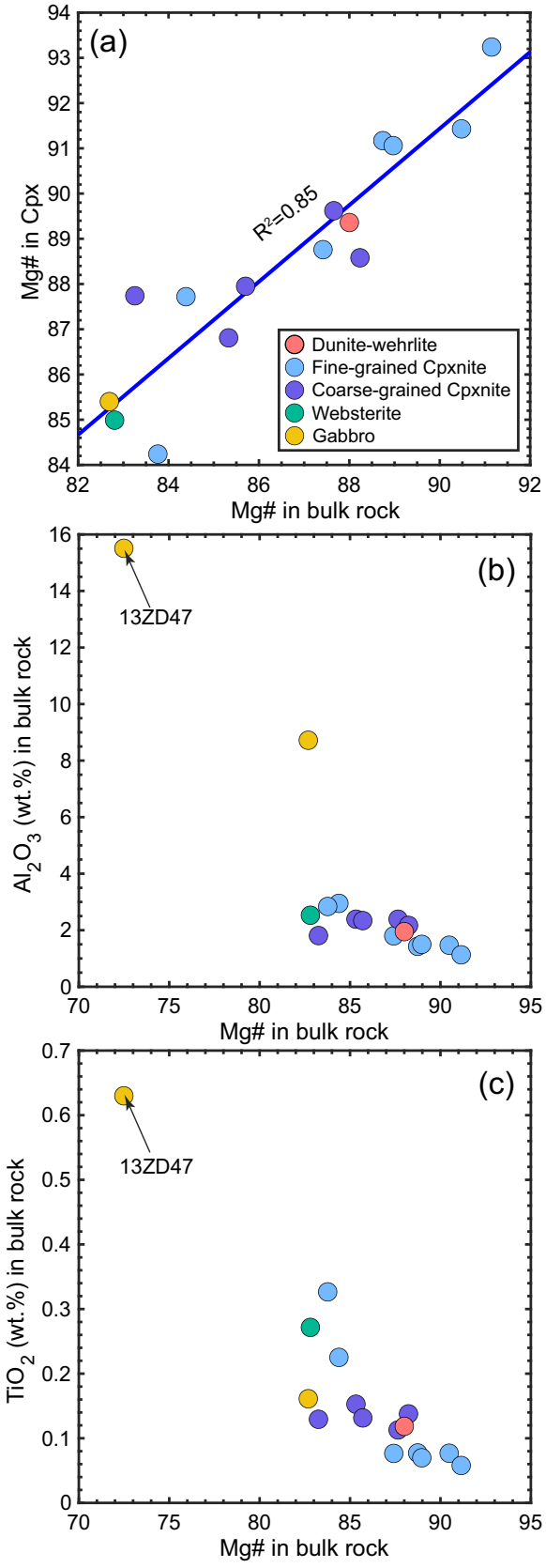

Fig. 4. Bulk rock major element compositions of the Zedong MTZ samples. Covariation diagrams illustrating (a) Mg# values between bulk rock and clinopyroxene in the same sample, (b) Al_2O_3 versus Mg#, and (c) TiO_2 versus Mg#.

Nearly all of the studied samples contain notably negative anomalies in Nb, Zr, and Hf, along with weakly negative anomalies in Ta and Ti (Fig. 5). The Zedong pyroxenitic samples exhibit analogous trends in MREE–HREE and high field strength elements (HFSE), with the patterns being subparallel to those found in Zedong gabbros. These pyroxenitic samples display more pronounced depletion in LREE compared with the Zedong gabbro (Fig. 5). Lastly, trace element patterns of websterite and gabbros from the Zedong MTZ fall within the range of the Zedong gabbros (Fig. 5).

4.2. Zircon SIMS U—Pb ages of the Zedong gabbro

Zircons were only separated from one gabbroic sample 13ZD47. The CL images and U—Pb dating results of 22 zircon grains are shown in Fig. S2.1 and listed in Table S2, respectively. These zircons display long-prism shapes and homogeneous internal textures, with weak to no oscillatory zoning (Fig. S2.1). Thorium and Uranium contents of these zircons are variable, with Th/U ratios higher than 0.1 (Fig. S2b), which is diagnostic of their magmatic origin (e.g., Grimes et al., 2009). In the Tera-Wassenburg Inverse Concordia diagrams, the analytical data yield a lower intercept age and weighted average ^{207}Pb-corrected $^{206}Pb/^{238}U$ age of 131.6 ± 0.9 Ma and 131.7 ± 0.9 Ma (MSWD = 0.5), respectively (Fig. 6).

4.3. Mineral major element compositions

Clinopyroxene is the dominant mineral phase in the Zedong pyroxenites and gabbros (Table S1). They exhibit primitive compositions characterized by high Mg# values (83–93), low Al_2O_3 contents (0.85–3.00 wt% for pyroxenites, 3.82 wt% for the olivine gabbro), TiO_2 (0.04–0.34 wt% for pyroxenites and 0.37 wt% for the olivine gabbro), and Na_2O (0.12–0.37 wt% for pyroxenites and 0.51 wt% for the olivine gabbro) (Fig. 7). The inverse correlations observed between Mg# and Al_2O_3, TiO_2, and Na_2O in clinopyroxene resemble the crystallization trend of a primitive melt before plagioclase saturation (e.g., Jagoutz et al., 2007; Koepke et al., 2009). Three samples of olivine clinopyroxenite (18JL04, 18JL06, and 18JL09) contain two families of clinopyroxenes with distinct compositions. One family features high Mg# values, and the other displays lower Mg# values (indicated by black dashed arrows in Fig. 7, and Table S1). Furthermore, most clinopyroxenes within the Zedong MTZ samples display normal zoning in major elements with cores having higher Mg# values alongside lower concentrations of Al_2O_3, Cr_2O_3, TiO_2, and Na_2O compared to their rims (Figs. S4.4 and Table S4). Such zoning patterns are indicative of fractional crystallization trend (e.g., Drouin et al., 2009; Zhang et al., 2021). The exception is that some clinopyroxenes within the websterite 18JRG04 present a contrasting zoning pattern, characterized by slightly lower core Mg# values (84.6 as opposed to 85.2 in, Figs. S4.5).

Olivine and orthopyroxene are present as interstitial phases within clinopyroxenites, except for the websterite 18JRG04. Due to severe secondary alteration, we only measured olivine relics within pyroxenites (Figs. S4.1c, d). They are characterized by high forsterite (Fo) contents (82–90) and low NiO contents (0.15–0.20 wt%) (Fig. S4.1c). Orthopyroxene is a minor phase among samples in this study, they have variable Mg# values and exhibit low contents of Al_2O_3 (1.09–2.09 wt%) and CaO (0.67–1.09 wt%) (Fig. S4.1a and Table S4).

In terms of aluminum-rich phases, both spinel and plagioclase are nearly absent in the pyroxenites (Table S1). Spinel is only found in four olivine-clinopyroxenite samples (18JL09,18JRG5–2, 23JRG1–1, and 23JRG5–1). Their spinel exhibits a Cr# value of 38–54 and a TiO_2 content of 0.14–0.84 wt%, which falls within the Zedong peridotite range (Table S4; e.g., Xiong et al., 2017). Plagioclase in the gabbros is completely altered (Appendix 1), which is further supported by their major element compositions (Table S4).

Within the pyroxenites, we observed scattered diopside grains along the grain boundaries, which have variable Mg# values (78–90) and

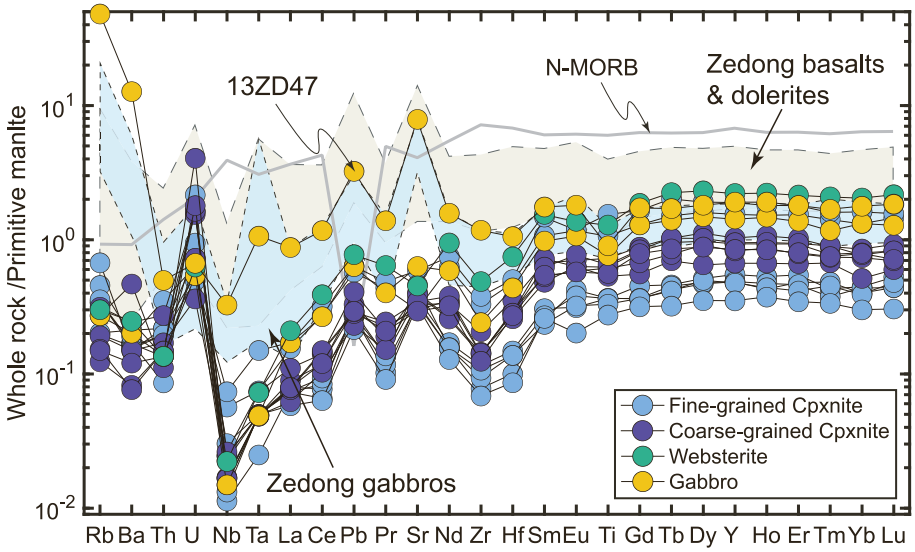

Fig. 5. Primitive mantle normalized trace element patterns of bulk rock compositions of clinopyroxenites, websterite, and gabbros from the Zedong ophiolite (Palme and O'Neill, 2014). Normal mid ocean ridge basalt (N-MORB) is included for reference (Sun and McDonough, 1989). Additionally, basalt, diabase, and gabbro data from the Zedong ophiolite are also shown for comparison (Liu et al., 2020b; Xiong et al., 2016; Zhang, 2014).

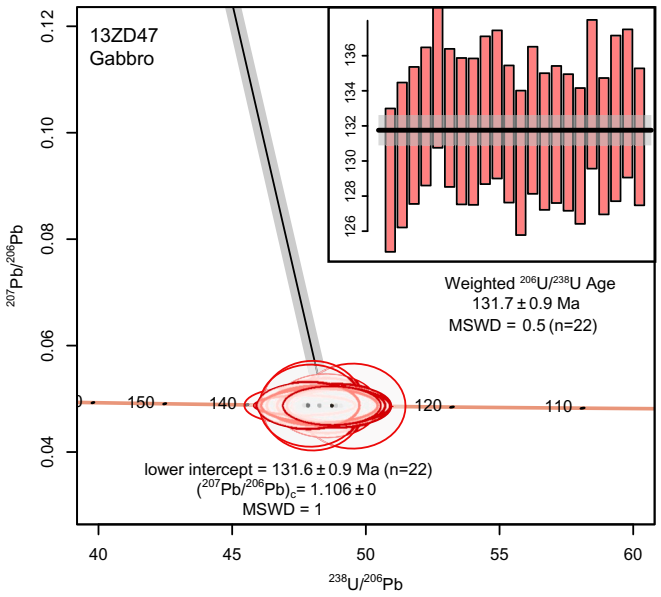

Fig. 6. Tera-Wassenburg Inverse Concordia diagram and weighted average ages for zircon grains from the mafic rock 13ZD47 in the Zedong ophiolite. Analytical errors are presented as 2σ.

extremely low concentrations of Al_2O_3 (0.42–1.07 wt%), Cr_2O_3 (0.02–0.21 wt%), TiO_2 (0.02–0.06 wt%), and Na_2O (0.04–0.30 wt%) (Table S4). Amphiboles are commonly identified in fine-grained clinopyroxenites and gabbros (Fig. 3d). In one clinopyroxenite (18JL06), the amphiboles are identified as tremolite or actinolite. They display Mg# values ranging from 77 to 90 and variable Al_2O_3 (0.21–1.73 wt%), Cr_2O_3 (0–0.24 wt%), TiO_2 (0.04–0.1 wt%), and Na_2O (0.06–0.23 wt%) (Fig. S4.2 and Table S4). Amphiboles in other clinopyroxenites and gabbros exhibit a trend from pargasite to magnesium-hornblende (Fig. S4.2). They feature low contents of SiO_2 (43.57–49.05 wt%), high Mg# (82–90) values, and high contents of Al_2O_3 (7.88–12.09 wt%), TiO_2 (0.34–1.44 wt%), and Na_2O (1.20–2.62 wt%) (Table S4).

4.4. Mineral trace element compositions

As depicted in Fig. 8, clinopyroxenes found in the Zedong MTZ display similar trace element patterns. They are characterized by depleted LREE and flat patterns in MREE to HREE (Fig. 8). These clinopyroxenes do not display any Eu anomalies relative to Sm and Gd, but have pronounced negative anomalies in Nb, Zr, Hf, and Ti (Fig. 8). Clinopyroxenes within the dunite-wehrlite, websterite, and gabbro exhibit elevated concentrations of trace elements (Fig. 8b) in comparison to those observed in clinopyroxenites (Fig. 8a). Additionally, clinopyroxene commonly display strong compositional zoning in trace elements with increasing contents of incompatible trace elements from their cores to rims (Figs. S4.6). Such a zonation is independent of compatibilities of different trace elements. In contrast, the clinopyroxene in the clinopyroxenite (18JN06) exhibit a reverse zoning (Fig. S4.7).

Due to small grain sizes of orthopyroxene, we were only able to measure orthopyroxenes in three samples. These orthopyroxenes exhibit LREE-depleted patterns without obvious Eu anomalies, except for the clinopyroxenite 18JN05 (Fig. S5.1a). In the primitive mantle normalized diagram, they display a positive Ti anomaly and mild positive Sr and Hf anomalies (Fig. S5.1b).

The trace element pattern of magnesio-hornblende mirrors that of clinopyroxene in the olivine clinopyroxenite 18JL04, but with overall abundances that are 2 to 3 times higher (Fig. S5.1c, d). Amphibole in this sample exhibits a depleted LREE and flat MREE to HREE pattern (Fig. S5.1c). In the spider diagram, it exhibits a strongly negative Zr anomaly and a mild negative Hf anomaly (Fig. S5.1d).

4.5. Cryptic variations of the Zedong MTZ

We conducted sampling along an NNE-SSW transect from the JRG massif along, aiming to explore cryptic variations, which indicate changes in mineral composition relative to stratigraphic position (Pallister and Hopson, 1981). This transect is perpendicular to the foliations of the magmatic layers, encompassing its entire structural thickness and constituting lithologies (Figs. 1b, c, and 9a). For this investigation, clinopyroxenes from the 16 samples, including pyroxenite, dunite, wehrlite, and gabbro, were analyzed for major and trace element concentrations (Fig. 9a). Vertical level is estimated from the distance to the section of mantle peridotite and is listed in Table S1. The JRG MTZ profile reveals at least two units of fractional crystallization

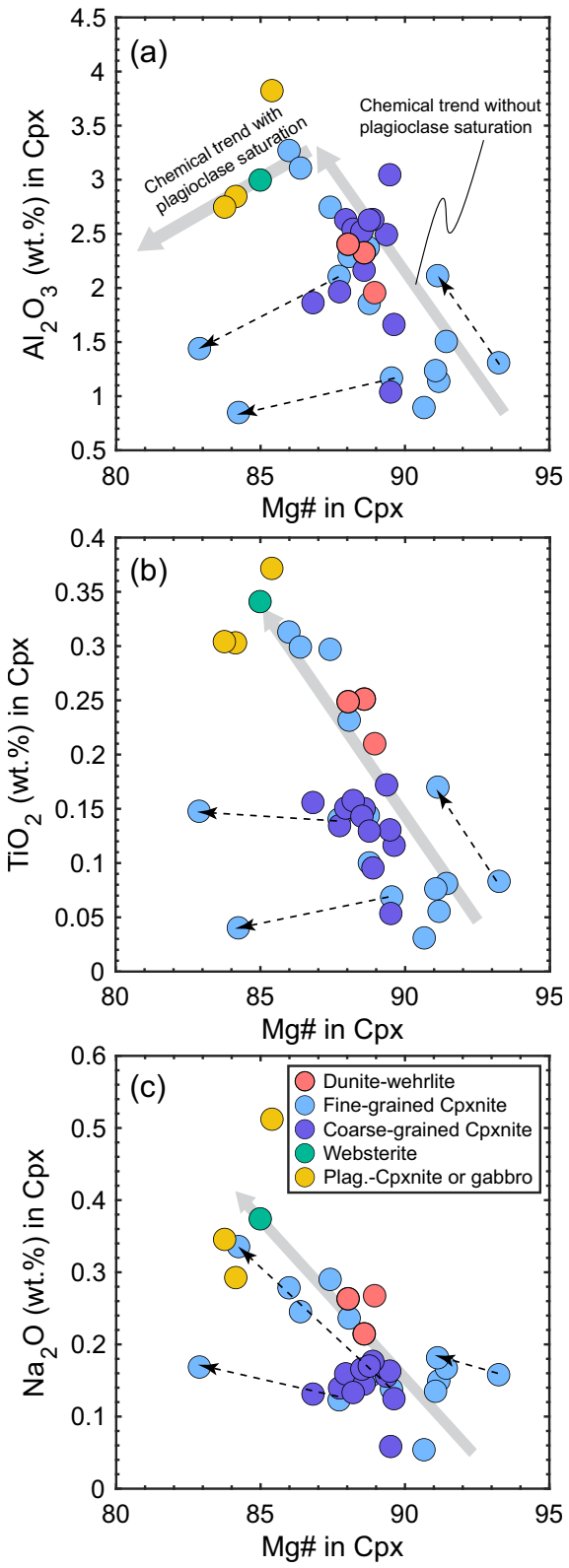

Fig. 7. Selected mineral major element compositions of clinopyroxenes in the studied pyroxenites and gabbros from the Zedong ophiolite. Clinopyroxene Al_2O_3 (a), TiO_2 (b), and Na_2O (c) plotted against Mg#. The differentiation trends of clinopyroxene within the Kohistan arc cumulates, characterized by increasing contents of Al_2O_3, TiO_2, and Na_2O as Mg# values decreasing until plagioclase saturation is reached (Bouilhol et al., 2015; Jagoutz et al., 2007), are presented for comparative analysis. Dashed arrows connect two generations of clinopyroxenes within one sample.

and replenishment, as evidenced by the zig-zag normal and reverse cryptic variation differentiation trends, and corresponding recurrence of dunite-wehrlite associations (Fig. 9). Within each magmatic unit, clinopyroxenes exhibit a decline in Mg# values and an increase in Al_2O_3, TiO_2, and incompatible trace elements (Figs. 9b–f). A notable exception is the coarse-grained clinopyroxenite 23JRG5 which has high Mg# and high Al_2O_3 contents (Fig. 9c). In summary, the Zedong pyroxenitic MTZ section displays episodic chemical variations and distinct breaks downsection in the major and trace element compositions of clinopyroxene (Fig. 9).

4.6. Temperature estimates for the Zedong clinopyroxenites

The estimation of closure temperatures was solely conducted for the Zedong F-Cpxnite samples due to the absence of orthopyroxene in both the C-Cpxnite and gabbroic samples. Assuming a pressure of 0.3 GPa, the determination of closure temperatures was based on the methods of Mg—Fe exchange between coexisting clinopyroxene and orthopyroxene, as well as the Ca solubility in orthopyroxene (Brey and Köhler, 1990). As a prerequisite for these thermodynamic calculations, the chemical equilibrium of an element of interest between the two pyroxenes was tested first. In Fig. S4.3, Fo values of olivine, Mg# values of orthopyroxene and amphibole were plotted against Mg# of clinopyroxene. Nearly all of our samples were plotted along the chemical equilibrium lines, suggesting Mg—Fe exchange equilibrium was established between these minerals. Similarly, the REE partition between the coexisting orthopyroxene and clinopyroxene were examined for the three samples (18JL04, 18JN05, and 18JRG04). We note the obvious disequilibrium REE distribution between clinopyroxene and orthopyroxene in the clinopyroxenite 18JN05, as evidenced by its distinct orthopyroxene REE pattern (Fig. S5.1a).

By excluding the sample 18JN05 (Fig. S4.1), the REE-based closure temperatures (Liang et al., 2013) of the Zedong MTZ samples span the range of 1165–1192 °C (n = 2), notably surpassing the closure temperature derived from major elements (T_{BKN} = 839–942 °C, n = 7; T_{Ca} = 903–1023 °C, n = 7). Detailed results are provided in Table S1.

4.7. Nd and Hf isotopic compositions

We conducted Neodymium and Hafnium isotopic analyses of 16 samples and 1 clinopyroxene separate, and the results are listed in Table S6. All of the samples display limited variations in $^{147}Sm/^{144}Nd$ (0.218–0.376), $^{143}Nd/^{144}Nd$ (0.513041–0.513196), $^{176}Lu/^{177}Hf$ (0.058–0.119), and $^{176}Hf/^{177}Hf$ (0.283194–0.283434). We calculated the initial $^{143}Nd/^{144}Nd$ and $^{176}Hf/^{177}Hf$ ratios, $\varepsilon_{Nd}(t)$ and $\varepsilon_{Hf}(t)$ values at 130 Ma, which corresponds to the formation age of both the Zedong ophiolite and other ophiolites along the YTSZ. Specifically, these values varied from 0.512813 to 0.512907 for $^{143}Nd/^{144}Nd$ ($\varepsilon_{Nd}(t)$ = +6.60 to +8.43) and 0.283051 to 0.283173 for $^{176}Hf/^{177}Hf$ ($\varepsilon_{Hf}(t)$ = +12.77 to +16.26) (Fig. 10). The Nd—Hf isotopic compositions of the Zedong MTZ rocks are more depleted than the range defined by typical of mafic rocks of from the YTO (Fig. 10).

5. Discussion

5.1. Geochronology of the Zedong gabbro

In this study, one gabbro (13ZD47), interbedded with fine-grained clinopyroxenite located at the top of the MTZ in the Jinlu profile (Fig. 1b), yielded an early Cretaceous age of 131.6 ± 0.9 Ma (Fig. 4). This age aligns with that of dolerite and gabbroic dikes intruding into the Zedong mantle peridotite (~ 130–128 Ma) (e.g., Chen et al., 2015; Xiong et al., 2016). Furthermore, a prior study on the zircon U—Pb ages of the Luobusa metamorphic sole has determined an age of 131.0 ± 1.2 Ma (Fig. 1a, Zhang et al., 2016a, 2016b), which is identical within uncertainty to the age of intruding dikes in the Zedong ophiolite.

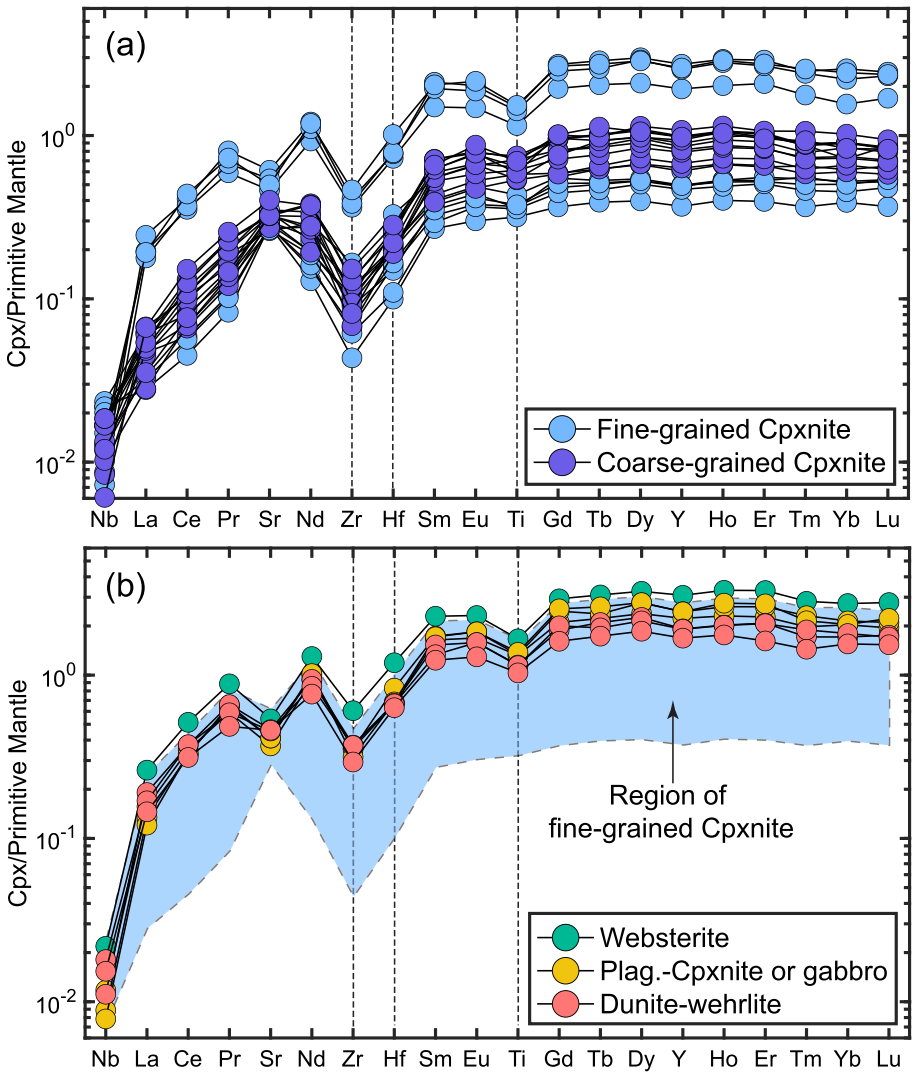

Fig. 8. Primitive mantle (Palme and O'Neill, 2014) normalized trace element patterns of clinopyroxenes from clinopyroxenites (a), websterite, dunite-wehrlite associations, and gabbros (b).

Consequently, we infer that the MTZ within the Zedong ophiolite was formed between 132 and 128 Ma, consistent with the age range of 132–120 Ma established in previous geochronological works in other YTSZ ophiolites (e.g., Liu et al., 2016; Liu et al., 2022).

In addition, the bulk rock trace element patterns of the Zedong MTZ rocks differ from those of the Zedong arc complex (Fig. 1b). The latter is characterized by LREE enriched patterns and older formation ages (~160–155 Ma, Zhang et al., 2014). Therefore, there is no genetic relationship between the Zedong MTZ and the Zedong arc complex (Fig. 1b).

5.2. *Differentiation sequence of the Zedong pyroxenitic MTZ*

The Zedong MTZ associations are characterized by the prevalence of clinopyroxene-rich lithologies, including clinopyroxenites, wehrlites, and websterites. The textures of the Zedong MTZ samples, displaying adcumulate to orthocumulate textures (Table S1), closely resemble those of crustal wehrlites observed in the Oman ophiolite (e.g., Akizawa et al., 2012; Koepke et al., 2009; Koga et al., 2001; Nicolle et al., 2016; Pallister and Hopson, 1981). These crustal wehrlites and pyroxenites are commonly interpreted as products of melt accumulation and/or melt-peridotite reaction at pressures near or below the plagioclase stability field (e.g., Benoit et al., 1999; Clénet et al., 2010; Nicolle et al., 2016).

Within the Zedong MTZ, we observed several continuous lithological variations, encompassing dunite, wehrlite, (olivine-) clinopyroxenite, websterite, and gabbro from the bottom to the top (Fig. 9a). The presence of olivine-rich intervals suggests the early crystallization of olivine. The limited occurrence of orthopyroxene and nearly absence of plagioclase in the MTZ sections, coupled with significantly decreasing Mg# values from clinopyroxenites towards websterite and gabbros (Fig. 7), indicate that orthopyroxene and plagioclase are late crystallizing phases. Consequently, the crystallization sequence within the Zedong MTZ follows the order of olivine, olivine + clinopyroxene, olivine + clinopyroxene +orthopyroxene/plagioclase. Amphibole represents the latest crystallizing phase in the clinopyroxenites and gabbros. This is evident from their peritectic relationships with clinopyroxenes (Fig. S1-S3 in Appendix 1), where clinopyroxenes react with the percolating melt to form amphiboles (e.g., Gillis and Meyer, 2001).

The crystallization sequence observed in the Zedong MTZ is not consistent with the fractionation of a dry MORB melt at MTZ pressures. At pressures prevalent at the MTZ (0.3–0.5 GPa), MORB is not expected to crystallize clinopyroxene until significant olivine and plagioclase have crystallized (e.g., Grove et al., 1992). Clinopyroxene in the Zedong MTZ display an increase in the contents of Al_2O_3 and TiO_2, coupled with a decrease in Mg# (Figs. 7a, b, and c). Similarly, olivine in the Zedong

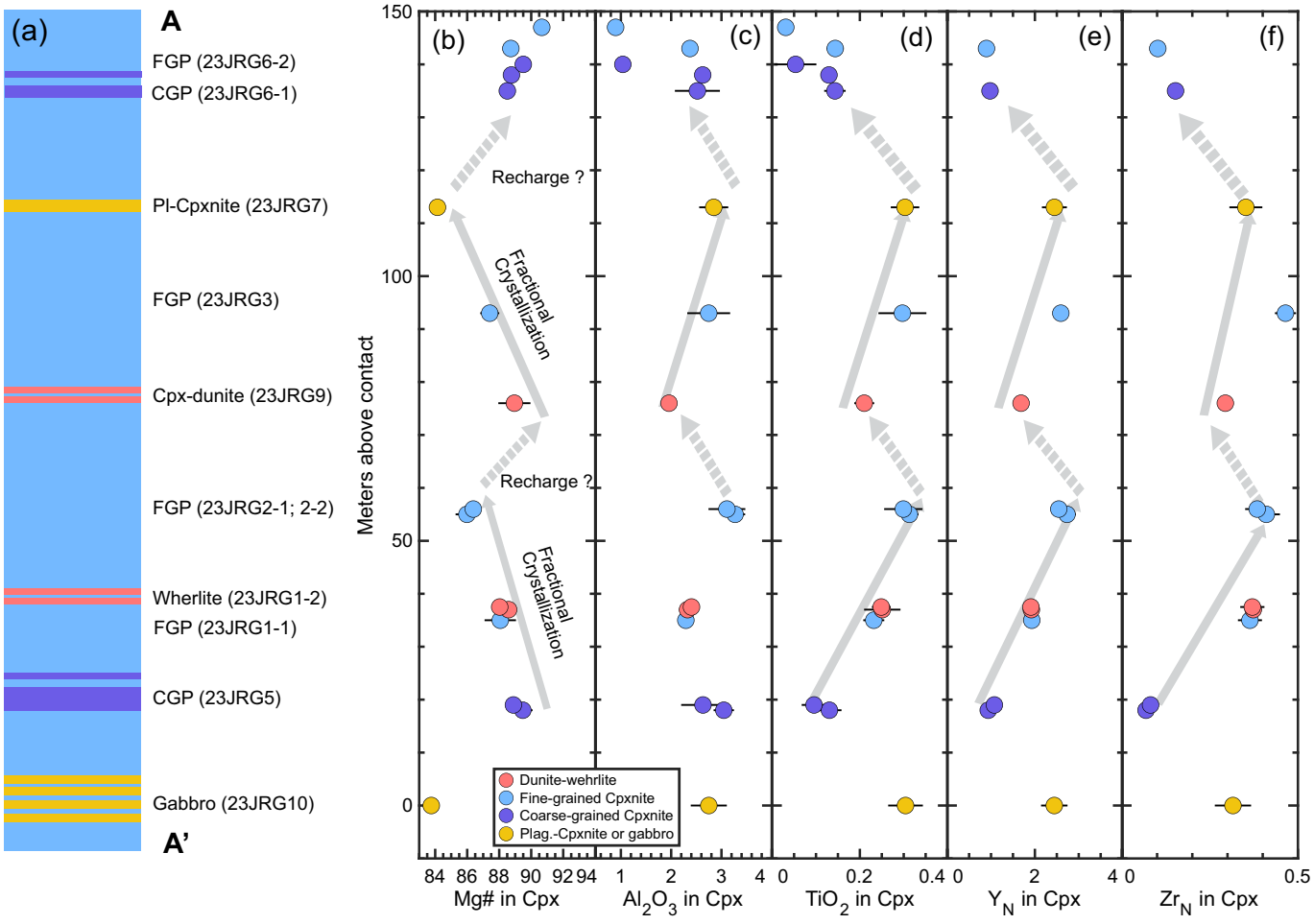

Fig. 9. Downsection plots illustrating the variation in lithology (a), Mg# values (b), Al_2O_3 (c) and TiO_2 contents (d), and primitive mantle normalized concentrations of Y (e) and Zr (f) in clinopyroxenes from the Zedong MTZ. The error bars represent the standard deviation (1σ). Abbreviations: F-Cpxnite: fine-grained clinopyroxenite; C-Cpxnite: coarse-grained clinopyroxenite; Pl-Cpxnite: plagioclase-clinopyroxenite; Cpx-dunite: clinopyroxene bearing dunite.

MTZ exhibits decrease in NiO and increase in MnO (Fig. S4.1c, d). These chemical evolution trends, combined with the consistently high Mg# values in clinopyroxene and high Fo contents in olivine, indicate that the Zedong MTZ was formed by differentiation of a primitive melt. In terms of Anorthite (An)-Diopside-Forsterite ternary phase diagram, the primitive melt should be plotted in the An-poor part of the olivine primary phase field, below the eutectic point (Hess, 1992). Such a depleted melt could be formed by partial melting of a clinopyroxene-poor lherzolite or harzburgite (e.g., Weaver et al., 2011). Moreover, presence of water delays plagioclase crystallization (e.g., Feig et al., 2006; Koepke et al., 2021; Nandedkar et al., 2014; Neave et al., 2019). Given the frequent presence of magmatic amphiboles in the studied samples (Figs. S1.1 to 1.3 and S4.2), we infer that the primary melt could be a hydrous melt depleted in Al_2O_3, TiO_2, and Na_2O. This hypothesis will be further tested in the following section using trace element data.

5.3. Nature of the parental melts

The Zedong MTZ samples consistently display LREE-depleted REE patterns for both bulk rock (Fig. 5) and clinopyroxene compositions (Fig. 8), suggesting they were derived from a depleted mantle source. In addition, the studied samples exhibit relatively uniform Nd—Hf isotopic compositions that are slightly displaced towards to a more depleted component compared to those of MORB and crustal rocks (i.e., basalts, diabases, and gabbros) from the whole YTSZ (Fig. 10). These observations strongly support the inference that the parental melt of the Zedong MTZ was formed by re-melting of a depleted source.

To further delve into the characteristics of the parental melts, we calculated the trace element patterns of the equilibrium melts. Here, we focused on Nb, Sr, REE, Zr, Hf and Ti contents in the calculated melts in equilibrium with clinopyroxene, orthopyroxene, and amphibole. Elements that could potentially have been altered by secondary processes were excluded from our analysis (U, Pb, Rb, and Ba; please refer to Figs. S3 for detailed information). Additionally, elements with concentrations falling below the detection limit (Th and Ta) were not considered (Table S5). The mineral-melt partition coefficients are from parameterized lattice models based on major element compositions of clinopyroxene, orthopyroxene, and amphibole (Shimizu et al., 2017; Sun and Liang, 2012, 2014; Sun, 2014). The modeling results and hydrous mineral-melt partition coefficients used in this study are provided in Table S7. Several conclusions can be drawn from the modeling results. Firstly, the calculated melts in equilibrium with clinopyroxenes are characterized by nearly flat REE patterns, gradually depleted patterns from HREE to MREE, strong depletion in Zr and Hf, and mild positive enrichments in Ti (Fig. 11a). These trace element patterns are different from those of the bulk rock compositions of the Zedong crustal rocks (Fig. 11a). Specially, negative anomalies of Zr and Hf were frequently observed in both bulk rocks and clinopyroxenes within the Zedong harzburgites and lherzolites (Xiong et al., 2016; Xiong et al., 2017). Partial melting of such Zr- and Hf-depleted peridotites in the Zedong ophiolite can produce melts with notable negative anomalies of Zr and Hf. Secondly, the trace element patterns of the calculated melts in

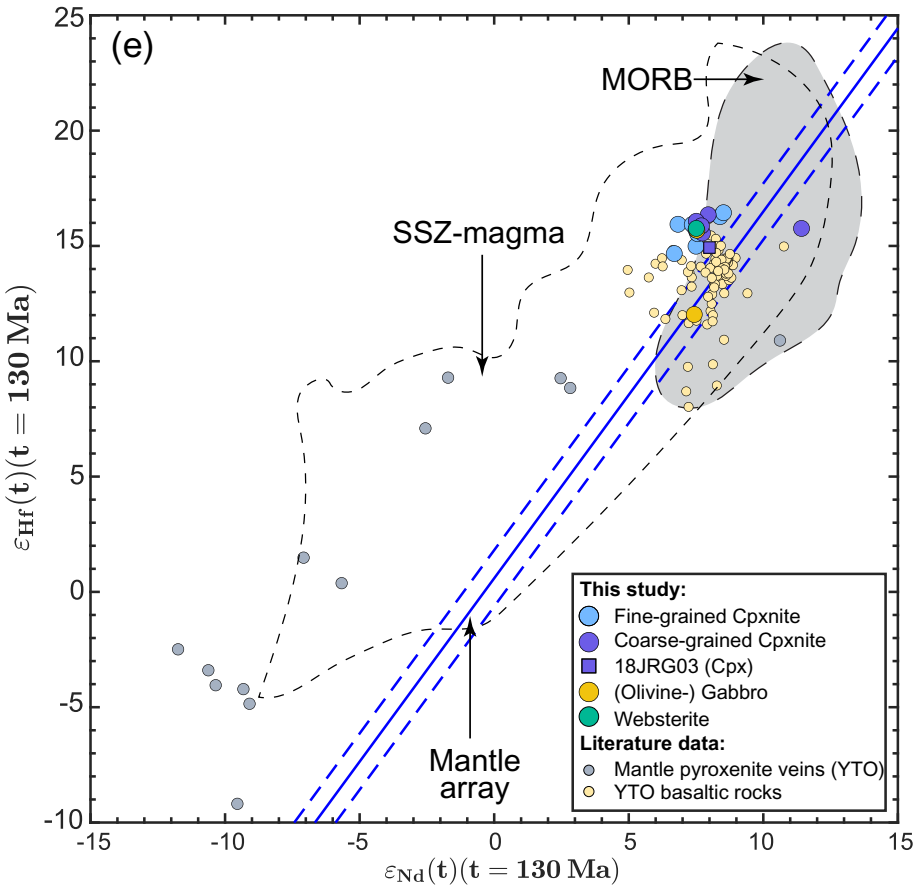

Fig. 10. ε_{Nd} and ε_{Hf} values for pyroxenites and gabbros in the Zedong MTZ at 130 Ma. Comparative ε_{Nd} and ε_{Hf} values for MORB (Salters et al., 2011; Stracke et al., 2003), island-arc volcanics from the GEOROC database (https://georoc.eu/georoc/new-start.asp), mafic rocks from the YTSZ (Liu et al., 2018; Xiong et al., 2016; Zhang et al., 2016a; Zhang et al., 2016b; Zhang et al., 2023b), pyroxenite veins from the YTSZ (Zhang et al., 2022), and the mantle array with 2 S.E. presented in blue lines (Willig et al., 2020). (For interpretation of the references to colour in this figure legend, the reader is referred to the web version of this article.)

equilibrium with clinopyroxene exhibit a distinct pattern compared to forearc basalts and boninites, suggesting a distinct origin for the Zedong MTZ in comparison to forearc basalts and boninites (Fig. 11b). Thirdly, the calculated melts in equilibrium with orthopyroxene in the clinopyroxenite 18JN05 and websterite 18JRG04 display enriched LREE patterns (Fig. 11c), which contrasts with the melts in equilibrium with clinopyroxene in the same sample. This suggests that orthopyroxenes within these two samples crystalized from more evolved melts.

Based on these observations, we infer that the infiltrating melts that form the Zedong MTZ could result from partial melting of a residual peridotite that is depleted in Al_2O_3, TiO_2, and Na_2O but with typical Nd—Hf isotopic ratios and trace element patterns similar to MORB. To further explore the characteristics of the mantle source, we employed a two-porosity melting model described in Liang and Parmentier (2010) to calculate trace element patterns in the aggregated melt that extracted through high-porosity channels towards the MTZ. For purpose of demonstration, we assume that the trace element concentrations of the starting peridotite are the same as the average concentrations in the depleted harzburgites and lherzolites from the region (Xiong et al., 2016, 2017; Zhang et al., 2014). This choice of the starting mantle is note unique, but it is adequate to represent the trace element patterns of the local mantle source. The partition coefficients under hydrous conditions and other modeling parameters are listed in Table S7. Fig. 10d displays the trace element concentrations of aggregated melts generated by 0–6% near fractional melting of the initial mantle peridotite. These aggregated melts have trace element patterns nearly identical to the most primitive melts in equilibrium with clinopyroxenes in the Zedong MTZ. The negative anomalies of Zr and Hf in the melt in equilibrium with clinopyroxene appear to have been inherited from a mantle source that is itself depleted in Zr and Hf.

5.4. Formation mechanism and broader implications of the Zedong MTZ

The Zedong pyroxenitic MTZ exhibits consistent evolutionary trends in major and trace element, where the contents of Al_2O_3, TiO_2, Na_2O, and incompatible trace elements in clinopyroxene increase with decreasing clinopyroxene Mg# (Figs. 7 and 12). These chemical variation trends are commonly attributed to fractional crystallization of a melt. However, the fractional crystallization process alone cannot explain the following observations: (1) the interbedded layers of clinopyroxenite, wehrlite, and dunite (Fig. 2), (2) the re-occurrences of olivine-rich layers across the MTZ profile (Fig. 9), and (3) existence of two families of clinopyroxenes with distinct compositions within the three samples (Fig. 7). Therefore, additional melt-rock reaction processes are needed to explain the observed evolutionary trends in major and trace elements within the Zedong MTZ.

To further explore the effect of fractional crystallization and melt-rock reaction on the chemical composition of the MTZ, we utilized the thermodynamic software AlphaMELTS 2 to investigate these processes (Ghiorso and Sack, 1995; Smith and Asimow, 2005). Fractional crystallization (FC) of a primitive melt and the other is the assimilation-fractional crystallization (AFC). In the AFC scenario, the primitive melt assimilates an evolved crystal mush in terms of trace element (i.e., 10% olivine +90 clinopyroxene, Table S7) while undergoing fractional crystallization. Employing the parameterized lattice modes for REE, Zr, Hf, and Ti (Sun, 2014) along with major element compositions obtained

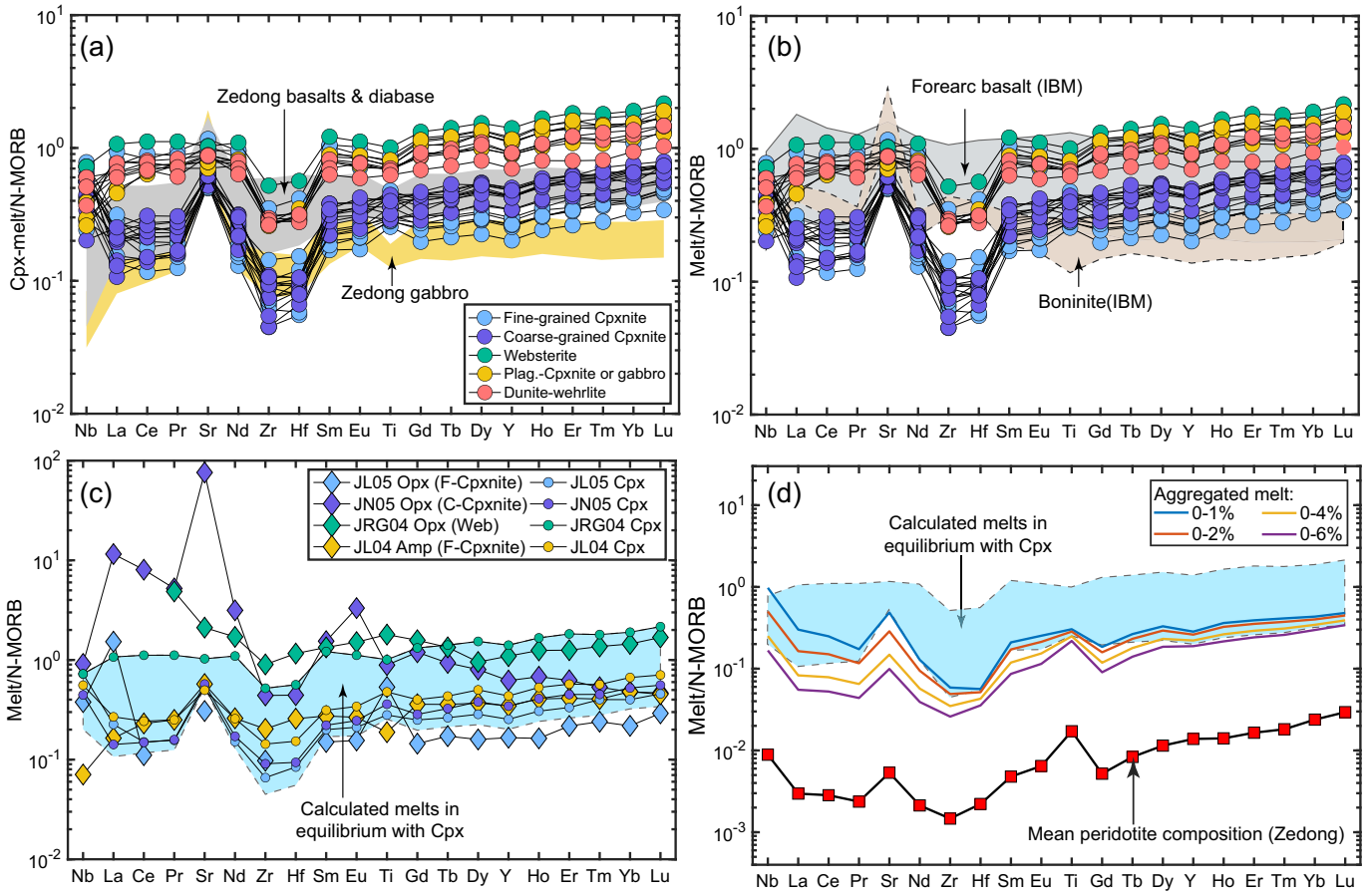

Fig. 11. (a) N-MORB normalized trace element patterns in calculated melts in equilibrium with clinopyroxenes (a, b), orthopyroxenes, and amphiboles (c) from the Zedong MTZ. Partition coefficients were determined using lattice strain models for clinopyroxene, orthopyroxene, and amphibole (Shimizu et al., 2017; Sun, 2014; Sun and Liang, 2012, 2014; Yao et al., 2012). The figures also include regions of the Zedong basalt, diabase, and gabbros for comparison (Liu et al., 2020b; Xiong et al., 2016; Zhang, 2014), along with forearc basalts and high-Ca boninite from the Izu-Boin-Mariana arc (Ishizuka et al., 2011; Reagan et al., 2010). (d) Trace element patterns of channel melts calculated by partial melting the mean residual lherzolite and harzburgite in the Zedong ophiolite (Xiong et al., 2016, 2017). Blue regions in panels (c) and (d) correspond to those in panel (a). See text for discussion. (For interpretation of the references to colour in this figure legend, the reader is referred to the web version of this article.)

from the modeling results, we can obtain the variations of major and trace elements in the cumulus phases. The bulk composition of a primitive melt can be approximated by using the most primitive basaltic lava found in the Zedong ophiolite, with an adjustment of MgO from 9.8 wt% to 12.0 wt%. This adjustment raised the Mg# of the melt from 68 to 75, situating it at the Mg-rich end of the spectrum of experimentally determined parental melts for Mid-Ocean Ridge Basalts (MORBs) (Table S7). The calculated liquidus temperature is ~1232 °C. Under a pressure of 0.3 GPa, fractional crystallization follows the sequence of olivine (Fo = 88–86), followed by olivine (Fo = 86–71) and clinopyroxene (Mg# = 90–79). The co-crystallization of olivine and clinopyroxene occurs at a decreasing temperature from 1184 °C to 1033 °C, with 95–49% melt remaining (Table S7 and Fig. 12). This temperature interval of coexistence of olivine and clinopyroxene is consistent with the REE closure temperature of the clinopyroxenites and websterites (Table S1).

Fractional crystallization successfully reproduces the subparallel trace element patterns depicted in Fig. 12a and the Mg#-Al_2O_3 diagram in Fig. 12c. However, it fails to capture the co-variation trends of Mg# and trace element contents in clinopyroxenes (Figs. 12d-f). Hence, we performed an AFC process at a pressure of 0.3 GPa and temperatures decreasing from 1233 to 1133 °C. Utilizing the same initial melt as in the FC modeling, we assumed the assimilation of 2 g/°C of olivine clinopyroxenite with evolved compositions (10% olivine and 90% clinopyroxene, Table S7). During the temperature decreasing, the primitive melt fractionates olivine and clinopyroxene with a high assimilation-to-crystallization ratio (r = 0.8). In comparison to the elemental evolution trends from the FC process (r = 0), the AFC process can accelerate the rate of melt enrichment in Al_2O_3 and trace elements (Fig. 12). This acceleration primarily depends on the on the compositions of the assimilated material. Assuming 25% fractionation of the melt, the AFC processes could account for both the subparallel trace element patterns (Fig. 12b) and the co-variation trends of Mg# and trace element contents in clinopyroxene (Figs. 12d-f).

Cryptic variations of the JRG stratigraphic section also support that both fractional crystallization and reaction between infiltrating melt and pre-existing crystal mush play an import role in building the formation of the MTZ. As shown in the Fig. 9, although the data is patchy, the variations of Mg#, Al_2O_3, and trace element contents in clinopyroxene from the JRG profile encompass the entire ranges defined by the Zedong MTZ (Figs. 9 and 12). Hence, the chemical variations along the profile are significant, which are likely characterized by zig-zag patterns, comprising both normal and reverse differentiation segments. The normal cryptic trends are characterized by a concurrent decrease in Mg# and increase in the contents of Al_2O_3, TiO_2, Na_2O, and trace elements (Fig. 9). These trends can be attributed to the fractionation of a primitive melt. A similar conclusion can also be drawn from the common occurrences of normal core-to-rim compositional zoning in clinopyroxene (Figs. S4.5 and 4.7). Notably, these normal cryptic trends, spanning approximately 35 m, exhibit a quite small scale compared with those of

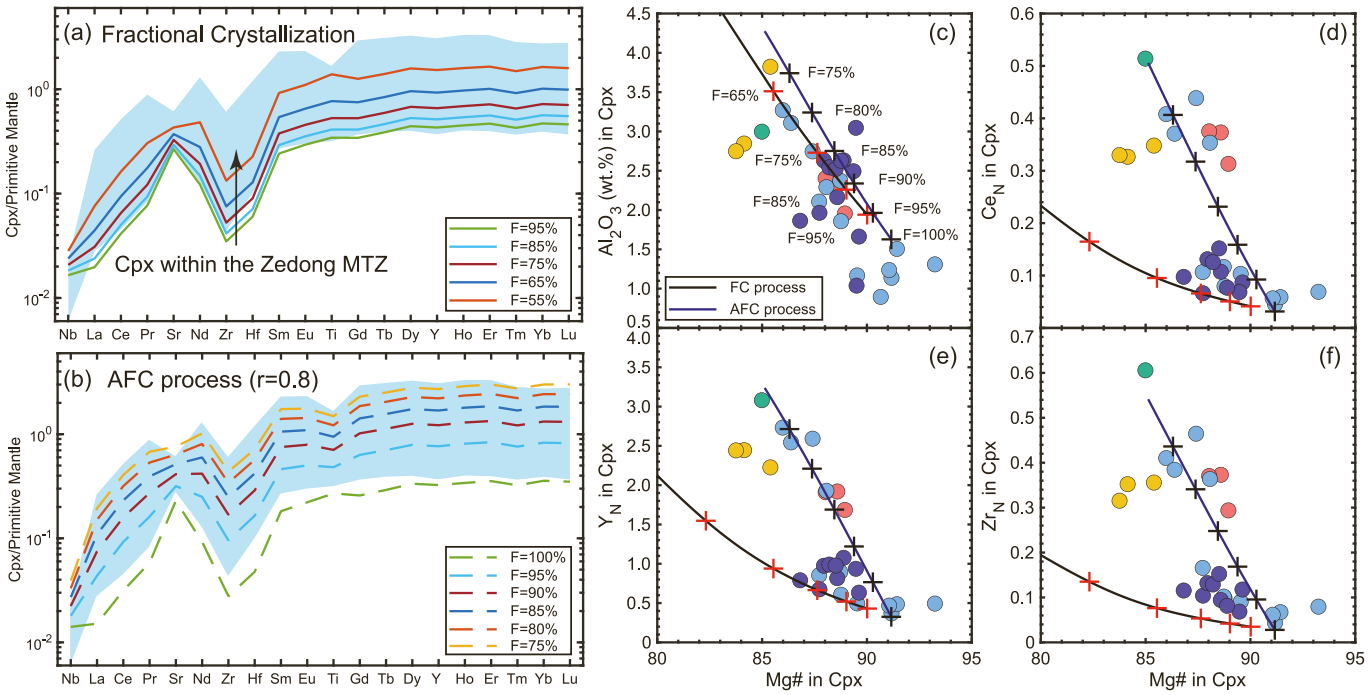

Fig. 12. (a) Numerical simulations of major and trace element compositions of clinopyroxene during fractional crystallization (FC) and assimilation-fractional crystallization (AFC) processes. The parameter 'r' represents the assimilated to crystallized mass ratio, and 'F' represents fractions of the remaining magma. Colored symbols correspond to those in Figs. 7–9. See text for details.

the Oman ophiolite, which extends over hundreds of meters (Rospabé et al., 2019). This discrepancy implies the Zedong MTZ was formed through crystallization of relatively small volumes of primitive magma. The emergence of reverse differentiation cryptic variation trends is sometimes related to recurrent olivine-rich intervals (i.e. clinopyroxene-bearing dunite 23JRG09 in Fig. 9), which could result from the replenishment of the primitive melt. Such a replenishment process likely involves melt-rock reaction between the primitive melts and pre-existing melt mush. The reactive nature of interstitial orthopyroxene-clinopyroxene-amphibole (Fig. 3b-d) and the coexistence of clinopyroxenes of contrasting Mg# values within the three samples (Fig. 7) can potentially be explained by the reaction between the intruding primitive melt (high Mg# melt) and the evolved, preexisting clinopyroxene-rich melt mush (low Mg# clinopyroxene). In addition, the limited occurrences of clinopyroxenes with reversal chemical zoning patterns also support this hypothesis (Figs. S4.4 and S4.6).

In summary, the present study highlights that the lithological and chemical variations of Zedong MTZ samples can be explained by episodic differentiation and replenishment of hydrous basaltic melts. This formation mechanism could account for a wide array of clinopyroxene-rich MTZ sequences in numerous ophiolites (e.g., Akizawa et al., 2012; Ceuleneer and Le Sueur, 2008; Karson et al., 1984; Koepke et al., 2009; Sano and Kimura, 2007) and ultramafic massifs around the world (e.g., Bouilhol et al., 2015; Jagoutz et al., 2007). In addition, the hydrous melts that building the Zedong MTZ were generated by re-melting previously depleted peridotites. This re-melting process can be reconciled by either a subduction initiation model (e.g., Dai et al., 2013; Xiong et al., 2016, 2017) or a subduction re-initiation model (e.g., Liu et al., 2022; Zhang et al., 2019). To further explore the tectonic settings, more structural, petrological, and geochemical studies on the Zedong ophiolite are necessary.

6. Conclusion

The comprehensive examination of the MTZ in the Zedong ophiolite, combining structural, petrological, and geochemical analyses, reveals the following key observations: (1) the chemical evolution trends documented in the clinopyroxene results from multiple stages of melt replenishments and fractional crystallization; (2) the parental melts of the MTZ samples are hydrous and contain low contents Al_2O_3, TiO_2, and Na_2O; (3) both the bulk rock Nd—Hf isotopic compositions and clinopyroxene trace element patterns suggest that the mantle source of the Zedong MTZ has experienced re-melting processes in a newly-forming subduction zone.

We proposed that both "subduction initiation" and "subduction re-initiation" models can account for these characteristics. The initiation of a subduction zone triggers the re-melting of previously depleted mantle peridotite, resulting in the formation of primitive hydrous basaltic melts. The diverse lithologies observed in the Zedong MTZ are attributed to fractional crystallization and repeated replenishment of these hydrous melts. Consequently, the architecture of the Zedong MTZ offers valuable lithological and chemical insights into the MTZ accretion processes at a paleo-spreading center.

CRediT authorship contribution statement

Zhen-Yu Zhang: Writing – review & editing, Writing – original draft, Visualization, Methodology, Investigation, Formal analysis, Data curation, Conceptualization. **Chuan-Zhou Liu:** Writing – review & editing, Methodology, Funding acquisition, Conceptualization. **Yan Liang:** Writing – review & editing, Funding acquisition, Conceptualization. **Liang-Liang Zhang:** Writing – review & editing, Formal analysis, Data curation. **Chang Zhang:** Writing – review & editing, Data curation. **Tong Liu:** Writing – review & editing, Data curation. **Bo-Da Liu:** Writing – review & editing. **Wei-Qi Zhang:** Writing – review & editing. **Yin-Zheng Lin:** Writing – review & editing, Visualization. **Wen-Bin Ji:** Writing – review & editing, Data curation.

Declaration of competing interest

All authors declare that they have no competing interests that could have appeared to influence the work reported in this paper.

Acknowledgements

The authors are grateful to Yue-Heng Yang, Shi-Tou Wu, Chao Huang, Di Zhang, Li-Hui Jia, and Jin-Hua Li for data acquisition, Bao-Jun Zhou, Zhen-Zhang, and Jia-Ning Zhu for their help during the field trip in Tibet. This work was supported by grants from the National Science Fund for Distinguished Young Scholars (42025201), the National Key Research and Development Project of China (2020YFA0714801), the Key Research Program of the Institute of Geology and Geophysics (IGGCAS-202202). Grants for Yan Liang were provided by the US National Science Foundation (OCE-1852088 and EAR-2147598).

Appendix A. Supplementary data

Supplementary data to this article can be found online at https://doi.org/10.1016/j.lithos.2024.107703.

References

Abily, B., Ceuleneer, G., 2013. The dunitic mantle-crust transition zone in the Oman ophiolite: Residue of melt-rock interaction, cumulates from high-MgO melts, or both? Geology 41 (1), 67–70.

Akizawa, N., Arai, S., 2009. Petrologic profile of peridotite layers under a possible Moho in the northern Oman ophiolite: An example from Wadi Fizh. J. Miner. Petrol. Sci. 104 (6), 389–394.

Akizawa, N., Arai, S., Tamura, A., 2012. Behavior of MORB magmas at uppermost mantle beneath a fast-spreading axis: an example from Wadi Fizh of the northern Oman ophiolite. Contrib. Mineral. Petrol. 164 (4), 601–625.

Arai, S., Takemoto, Y., 2007. Mantle wehrlite from Hess deep as a crystal cumulate from an ultra-depleted primary melt in East Pacific rise. Geophys. Res. Lett. 34 (8).

Bağci, U., Parlak, O., Höck, V., 2005. Whole-rock and mineral chemistry of cumulates from the Kızıldağ (Hatay) ophiolite (Turkey): clues for multiple magma generation during crustal accretion in the southern Neotethyan Ocean. Mineral. Mag. 69 (1), 53–76.

Batanova, V.G., Pertsev, A.N., Kamenetsky, V.S., Ariskin, A.A., Mochalov, A.G., Sobolev, A.V., 2005. Crustal Evolution of Island-Arc Ultramafic Magma: Galmoenan Pyroxenite–Dunite Plutonic Complex, Koryak Highland (Far East Russia). J. Petrol. 46 (7), 1345–1366.

Benn, K., Nicolas, A., Reuber, I., 1988. Mantle—crust transition zone and origin of wehrlitic magmas: evidence from the Oman ophiolite. Tectonophysics 151 (1–4), 75–85.

Benoit, M., Ceuleneer, G., Polvé, M., 1999. The remelting of hydrothermally altered peridotite at mid-ocean ridges by intruding mantle diapirs. Nature 402 (6761), 514–518. https://doi.org/10.1038/990073.

Boudier, F., Nicolas, A., 1995. Nature of the Moho transition zone in the Oman ophiolite. J. Petrol. 36 (3), 777–796.

Bouilhol, P., Schmidt, M.W., Burg, J.-P., 2015. Magma transfer and Evolution in Channels within the Arc Crust: the Pyroxenitic Feeder Pipes of Sapat (Kohistan, Pakistan). J. Petrol. 56 (7), 1309–1342.

Brey, G.P., Köhler, T., 1990. Geothermobarometry in four-phase lherzolites II. New thermobarometers, and practical assessment of existing thermobarometers. J. Petrol. 31 (6), 1353–1378.

Ceuleneer, G., Le Sueur, E., 2008. The Trinity ophiolite (California): the strange association of fertile mantle peridotite with ultra-depleted crustal cumulates. Bulletin de la Société Géologique de France 179 (5), 503–518. https://doi.org/10.2113/gssgfbull.179.5.503.

Chen, Y.-H., Yang, J.-S., Zhang, L., XIong, F.-H., 2015. Lai S-M (2015) Mineralogical study of the hornblende gabbro in Zetang ophiolite, southern Tibet, and its genetic implications. Geol. China 42 (5), 1421–1442 (in Chinese with English abstract). http://geochina.cgs.gov.cn/en/article/id/20150516.

Clénet, H., Ceuleneer, G., Pinet, P., Abily, B., Daydou, Y., Harris, E., Amri, I., Dantas, C., 2010. Thick sections of layered ultramafic cumulates in the Oman ophiolite revealed by an airborne hyperspectral survey: Petrogenesis and relationship to mantle diapirism. Lithos 114 (3), 265–281.

Dai, J., Wang, C., Polat, A., Santosh, M., Li, Y., Ge, Y., 2013. Rapid forearc spreading between 130 and 120 Ma: evidence from geochronology and geochemistry of the Xigaze ophiolite, southern Tibet. Lithos 172, 1–16.

Dick, H.J.B., Natland, J.H., 1996. Late-Stage Melt Evolution and Transport in the Shallow Mantle beneath the East Pacific Rise1. Proceedings of the Ocean Drilling Program, Scientific Results 147, 32.

Dick, H.J.B., Lissenberg, C.J., Warren, J.M., 2010. Mantle Melting, Melt Transport, and delivery beneath a Slow-Spreading Ridge: the Paleo-MAR from 23°15′N to 23°45′N. J. Petrol. 51 (1–2), 425–467.

Drouin, M., Godard, M., Ildefonse, B., Bruguier, O., Garrido, C.J., 2009. Geochemical and petrographic evidence for magmatic impregnation in the oceanic lithosphere at Atlantis Massif, Mid-Atlantic Ridge (IODP Hole U1309D, 30°N). Chem. Geol. 264 (1), 71–88.

Feig, S.T., Koepke, J., Snow, J.E., 2006. Effect of water on tholeiitic basalt phase equilibria: an experimental study under oxidizing conditions. Contrib. Mineral. Petrol. 152 (5), 611–638.

Ghiorso, M.S., Sack, R.O., 1995. Chemical mass transfer in magmatic processes IV. A revised and internally consistent thermodynamic model for the interpolation and extrapolation of liquid-solid equilibria in magmatic systems at elevated temperatures and pressures. Contrib. Mineral. Petrol. 119 (2–3), 197–212.

Gillis, K.M., Meyer, P.S., 2001. Metasomatism of oceanic gabbros by late stage melts and hydrothermal fluids: evidence from the rare earth element composition of amphiboles. Geochem. Geophys. Geosyst. 2 (3).

Girardeau, J., Francheteau, J., 1993. Plagioclase-wehrlites and peridotites on the East Pacific rise (Hess deep) and the Mid-Atlantic Ridge (DSDP Site 334): evidence for magma percolation in the oceanic upper mantle. Earth Planet. Sci. Lett. 115 (1), 137–149.

Girardeau, J., Mercier, J.C.C., Xibin, W., 1985. Petrology of the mafic rocks of the Xigaze ophiolite, Tibet. Contributions to Mineralogy and Petrology 90 (4), 309–321.

Grimes, C.B., John, B.E., Cheadle, M.J., Mazdab, F.K., Wooden, J.L., Swapp, S., Schwartz, J.J., 2009. On the occurrence, trace element geochemistry, and crystallization history of zircon from in situ ocean lithosphere. Contrib. Mineral. Petrol. 158 (6), 757–783.

Grove, T.L., Kinzler, R.J., Bryan, W.B., 1992. Fractionation of mid-ocean ridge basalt (MORB) in: Mantle flow and melt generation at mid-ocean ridges, 71, pp. 281–310.

Guilmette, C., Hébert, R., Wang, C., Villeneuve, M., 2009. Geochemistry and geochronology of the metamorphic sole underlying the Xigaze Ophiolite, Yarlung Zangbo Suture Zone, South Tibet. Lithos 112 (1–2), 149–162.

Guilmette, C., Hébert, R., Dostal, J., Indares, A., Ullrich, T., Bédard, É., Wang, C., 2012. Discovery of a dismembered metamorphic sole in the Saga ophiolitic mélange, South Tibet: Assessing an early cretaceous disruption of the Neo-Tethyan supra-subduction zone and consequences on basin closing. Gondw. Res. 22 (2), 398–414.

Hébert, R., Bezard, R., Guilmette, C., Dostal, J., Wang, C.S., Liu, Z.F., 2012. The Indus–Yarlung Zangbo ophiolites from Nanga Parbat to Namche Barwa syntaxes, southern Tibet: First synthesis of petrology, geochemistry, and geochronology with incidences on geodynamic reconstructions of Neo-Tethys. Gondw. Res. 22 (2), 377–397.

Hess, P.C., 1992. Phase Equilibria Constraints on the Origin of Ocean Floor Basalts. Mantle Flow and Melt Generation at Mid-Ocean Ridges, pp. 67–102.

Ishizuka, O., Tani, K., Reagan, M.K., Kanayama, K., Umino, S., Harigane, Y., Sakamoto, I., Miyajima, Y., Yuasa, M., Dunkley, D.J., 2011. The timescales of subduction initiation and subsequent evolution of an oceanic island arc. Earth Planet. Sci. Lett. 306 (3–4), 229–240.

Jagoutz, O., Müntener, O., Ulmer, P., Pettke, T., Burg, J.-P., Dawood, H., Hussain, S., 2007. Petrology and Mineral Chemistry of lower Crustal Intrusions: the Chilas complex, Kohistan (NW Pakistan). J. Petrol. 48 (10), 1895–1953.

Jousselin, D., Nicolas, A., Boudier, F., Reisberg, L., Henri, M., Nicolle, M., 2021. Formation of the Moho transition zone in the Oman ophiolite, and comparison with sub-Moho melt lenses at fast spreading ridges. Tectonophysics 821, 229148.

Karson, J.A., Collins, J.A., Casey, J.F., 1984. Geologic and seismic velocity structure of the crust/mantle transition in the Bay of Islands Ophiolite complex. J. Geophys. Res. Solid Earth 89 (B7), 6126–6138.

Kelemen, P.B., Kikawa, E., Miller, D.J., Party, S.S., 2007. Leg 209 summary: Processes in a 20-km-thick conductive boundary layer beneath the Mid-Atlantic Ridge, 14–16 N. Proc. Ocean Drill. Program Sci. Results 209, 1–33.

Koepke, J., Schoenborn, S., Oelze, M., Wittmann, H., Feig, S.T., Hellebrand, E., Boudier, F., Schoenberg, R., 2009. Petrogenesis of crustal wehrlites in the Oman ophiolite: experiments and natural rocks. Geochem. Geophys. Geosyst. 10 (10).

Koepke, J., Feig, S.T., Berndt, J., Neave, D.A., 2021. Wet magmatic processes during the accretion of the deep crust of the Oman Ophiolite paleoridge: phase diagrams and petrological records. Tectonophysics 817, 229051.

Koga, K.T., Kelemen, P.B., Shimizu, N., 2001. Petrogenesis of the crust-mantle transition zone and the origin of lower crustal wehrlite in the Oman ophiolite. Geochem. Geophys. Geosyst. 2, 1038. https://doi.org/10.1029/2000GC000132.

Lai, S.-M., Yang, J.-S., Xiong, F.-H., Liu, Z., Tian, Y.-Z., Xu, X.-Z., Zhou, W.-D., Zhang, L., Chen, Y.-H., Gao, J., 2015. Mineralogy and PGE features of Zedang peridotites in eastern Yarlung Zangbo suture, Tibet. Geology in China 42 (5), 1515–1534 (in Chinese with English abstract). http://geochina.cgs.gov.cn/cn/article/id/20150522.

Li, Y., Li, R., Yang, S., Zhang, J., Yang, J., 2022. Crust sequences of the Xigaze ophiolite in South Tibet: the water effect on crust accretion at a slow-spreading oceanic ridge and its implications. Lithos 106804.

Lian, D., Yang, J., Robinson, P.T., Liu, F., Xiong, F., Zhang, L., Gao, J., Wu, W., 2016. Tectonic Evolution of the Western Yarlung Zangbo Ophiolitic Belt, Tibet: Implications from the Petrology, Mineralogy, and Geochemistry of the Peridotites. J. Geol. 124 (3), 353–376.

Liang, Y., Parmentier, E.M., 2010. A Two-Porosity double Lithology Model for Partial Melting, Melt Transport and Melt–rock Reaction in the Mantle: Mass Conservation Equations and Trace Element Transport. J. Petrol. 51 (1–2), 125–152.

Liang, F.-H., Xu, Z.-Q., Ba, D.-Z., Xu, X.-Z., Liu, F., Xiong, F.H., Ji, Y., 2011. Tectonic occurrence and emplacement mechanism of ophiolites from Luobusha-Zedang, Tibet. Acta Petrologica Sinica 27 (11), 3255–3268 (in Chinese with English abstract). http://www.ysxb.ac.cn/article/id/aps_20111108.

Liang, Y., Sun, C., Yao, L., 2013. A REE-in-two-pyroxene thermometer for mafic and ultramafic rocks. Geochim. Cosmochim. Acta 102, 246–260.

Liu, C.-Z., Wu, F.-Y., Wilde, S.A., Yu, L.-J., Li, J.-L., 2010. Anorthitic plagioclase and pargasitic amphibole in mantle peridotites from the Yungbwa ophiolite (southwestern Tibetan Plateau) formed by hydrous melt metasomatism. Lithos 114 (3), 413–422.

Liu, C.-Z., Zhang, C., Yang, L.-Y., Zhang, L.-L., Ji, W.-Q., Wu, F.-Y., 2014. Formation of gabbronorites in the Purang ophiolite (SW Tibet) through melting of hydrothermally altered mantle along a detachment fault. Lithos 205, 127–141.
Liu, T., Wu, F.-Y., Zhang, L.-L., Zhai, Q.-G., Liu, C.-Z., Ji, W.-B., Zhang, C., Xu, Y., 2016. Zircon U-Pb geochronological constraints on rapid exhumation of the mantle peridotite of the Xigaze ophiolite, southern Tibet. Chem. Geol. 443, 67–86.
Liu, T., Wu, F.-Y., Liu, C.-Z., Tribuzio, R., Ji, W.-B., Zhang, C., Xu, Y., Zhang, W.-Q., 2018. Variably evolved gabbroic intrusions within the Xigaze ophiolite (Tibet): new insights into the origin of ophiolite diversity. Contrib. Mineral. Petrol. 173 (11), 91.
Liu, T., Liu, C.-Z., Wu, F.-Y., Dick, H.J., Ji, W.-B., Zhang, C., Zhang, W.-Q., Zhang, Z.-Y., Xu, Y., 2020a. The Xigaze ophiolite: fossil ultraslow-spreading ocean lithosphere in the Tibetan Plateau. J. Geol. Soc. London.
Liu, W., Zhong, Y., Sun, Z., Yakymchuk, C., Gu, M., Tang, G., Zhong, L., Cao, H., Liu, H., Xia, B., 2020b. The late Jurassic Zedong ophiolite: a remnant of subduction initiation within the Yarlung Zangbo Suture Zone (southern Tibet) and its tectonic implications. Gondw. Res. 78, 172–188.
Liu, C.-Z., Wu, F.-Y., Liu, T., Zhang, C., Zhang, W.-Q., Zhang, Z.-Y., Zhang, Z., Wei, W., Lin, Y.-Z., 2022. An origin of ultraslow spreading ridges for the Yarlung-Tsangpo ophiolites. Fundamental Research 2 (1), 74–83.
Nandedkar, R.H., Ulmer, P., Müntener, O., 2014. Fractional crystallization of primitive, hydrous arc magmas: an experimental study at 0.7 GPa. Contrib. Mineral. Petrol. 167 (6), 1015.
Neave, D.A., Namur, O., Shorttle, O., Holtz, F., 2019. Magmatic evolution biases basaltic records of mantle chemistry towards melts from recycled sources. Earth Planet. Sci. Lett. 520, 199–211.
Nicolas, A., Girardeau, J., Marcoux, J., Dupre, B., Xibin, W., Yougong, C., Haixiang, Z., Xuchang, X., 1981. The Xigaze ophiolite (Tibet): a peculiar oceanic lithosphere. Nature 294, 414.
Nicolle, M., Jousselin, D., Reisberg, L., Bosch, D., Stephant, A., 2016. Major and trace element and Sr and Nd isotopic results from mantle diapirs in the Oman ophiolite: Implications for off-axis magmatic processes. Earth Planet. Sci. Lett. 437, 138–149.
Pallister, J.S., Hopson, C.A., 1981. Samail Ophiolite plutonic suite: Field relations, phase variation, cryptic variation and layering, and a model of a spreading ridge magma chamber. J. Geophys. Res. Solid Earth 86 (B4), 2593–2644.
Palme, H., O'Neill, H.S.C., 2014. 3.1 - Cosmochemical estimates of Mantle Composition. In: Holland, H.D., Turekian, K.K. (Eds.), Treatise on Geochemistry (Second Edition), Vol. Elsevier, Oxford, pp. 1–39.
Reagan, M.K., Ishizuka, O., Stern, R.J., Kelley, K.A., Ohara, Y., Blichert-Toft, J., Bloomer, S.H., Cash, J., Fryer, P., Hanan, B.B., Hickey-Vargas, R., Ishii, T., Kimura, J.-I., Peate, D.W., Rowe, M.C., Woods, M., 2010. Fore-arc basalts and subduction initiation in the Izu-Bonin-Mariana system. Geochem. Geophys. Geosyst. 11, Q03X12. https://doi.org/10.1029/2009GC002871.
Rospabé, M., Benoit, M., Ceuleneer, G., Kaczmarek, M.-A., Hodel, F., 2019. Melt hybridization and metasomatism triggered by syn-magmatic faults within the Oman ophiolite: a clue to understand the genesis of the dunitic mantle-crust transition zone. Earth Planet. Sci. Lett. 516, 108–121.
Salters, V.J.M., Mallick, S., Hart, S.R., Langmuir, C.E., Stracke, A., 2011. Domains of depleted mantle: New evidence from hafnium and neodymium isotopes. Geochem. Geophys. Geosyst. 12 (8), Q8001.
Sanfilippo, A., Dick, H.J., Ohara, Y., 2013. Melt–rock reaction in the mantle: mantle troctolites from the Parece Vela ancient back-arc spreading center. J. Petrol. 54 (5), 861–885.
Sano, S., Kimura, J.-I., 2007. Clinopyroxene REE Geochemistry of the Red Hills Peridotite, New Zealand: Interpretation of Magmatic Processes in the Upper Mantle and in the Moho transition Zone. J. Petrol. 48 (1), 113–139.
Saper, L., Liang, Y., 2014. Formation of plagioclase-bearing peridotite and plagioclase-bearing wehrlite and gabbro suite through reactive crystallization: an experimental study. Contrib. Mineral. Petrol. 167 (3), 1–16. https://doi.org/10.1007/s00410-014-0985-7.
Shimizu, K., Liang, Y., Sun, C., Jackson, C.R., Saal, A.E., 2017. Parameterized lattice strain models for REE partitioning between amphibole and silicate melt. Am. Mineral. 102 (11), 2254–2267. https://doi.org/10.2138/am-2017-6110.
Smith, P.M., Asimow, P.D., 2005. Adiabat_1ph: a new public front-end to the MELTS, pMELTS, and pHMELTS models. Geochem. Geophys. Geosyst. 6, Q02004. https://doi.org/10.1029/2004GC000816.
Ss, Sun, McDonough, W.F., 1989. Chemical and isotopic systematics of oceanic basalts: implications for mantle composition and processes. Geol. Soc. Lond. Spec. Publ. 42 (1), 313–345.
Stracke, A., Bizimis, M., Salters, V.J., 2003. Recycling oceanic crust: Quantitative constraints. Geochem. Geophys. Geosyst. 4 (3), 8003. https://doi.org/10.1029/2001GC000223.
Sun, C., 2014. Trace Element Partitioning in Mantle Minerals with Applications to Subsolidus Re-Equilibration and Thermobarometry. PhD thesis. https://bruknow.library.brown.edu/discovery.
Sun, C., Liang, Y., 2012. Distribution of REE between clinopyroxene and basaltic melt along a mantle adiabat: effects of major element composition, water, and temperature. Contrib. Mineral. Petrol. 163 (5), 807–823.
Sun, C., Liang, Y., 2014. An assessment of subsolidus re-equilibration on REE distribution among mantle minerals olivine, orthopyroxene, clinopyroxene, and garnet in peridotites. Chem. Geol. 372 (0), 80–91.
Takazawa, E., Abe, N., Seyler, M., Meurer, W.P., Kelemen, P., 2007. Hybridization of dunite and gabbroic materials in Hole 1271B from Mid-Atlantic Ridge 15 N: Implications for melt flow and reaction in the upper mantle. In: Proc ODP, Sci Results, vol. 209. Ocean Drilling Program College Station, TX, pp. 1–23.
Tamura, A., Arai, S., Ishimaru, S., Andal, E.S., 2008. Petrology and geochemistry of peridotites from IODP Site U1309 at Atlantis Massif, MAR 30°N: micro- and macro-scale melt penetrations into peridotites. Contrib. Mineral. Petrol. 155 (4), 491–509. https://doi.org/10.1007/s00410-007-0254-0.
Villiger, S., Müntener, O., Ulmer, P., 2007. Crystallization pressures of mid-ocean ridge basalts derived from major element variations of glasses from equilibrium and fractional crystallization experiments. J. Geophys. Res. Solid Earth 112, B01202. https://doi.org/10.1029/2006JB004342.
Weaver, S.L., Wallace, P.J., Johnston, A.D., 2011. A comparative study of continental vs. intraoceanic arc mantle melting: Experimentally determined phase relations of hydrous primitive melts. Earth Planet. Sci. Lett. 308 (1), 97–106.
Willig, M., Stracke, A., Beier, C., Salters, V.J.M., 2020. Constraints on mantle evolution from Ce-Nd-Hf isotope systematics. Geochim. Cosmochim. Acta 272, 36–53.
Xiong, Q., Griffin, W.L., Zheng, J.-P., O'Reilly, S.Y., Pearson, N.J., Xu, B., Belousova, E. A., 2016. Southward trench migration at ~130–120 Ma caused accretion of the Neo-Tethyan forearc lithosphere in Tibetan ophiolites. Earth Planet. Sci. Lett. 438, 57–65.
Xiong, Q., Griffin, W.L., Zheng, J.P., Pearson, N.J., O'Reilly, S.Y., 2017. Two-layered oceanic lithospheric mantle in a Tibetan ophiolite produced by episodic subduction of Tethyan slabs. Geochem. Geophys. Geosyst. 18 (3), 1189–1213.
Xiong, Q., Dai, H.-K., Zheng, J.-P., Griffin, W.L., Zheng, H.-D., Wang, L., Reilly, S.Y.O., 2022. Vertical depletion of ophiolitic mantle reflects melt focusing and interaction in sub-spreading-center asthenosphere. Nat. Commun. 13 (1).
Yang, K., Dai, J., Shen, J., Debret, B., 2024. Melting processes, cooling rates, and tectonic settings of the Neo-Tethyan mantle: the in-situ mineral chemical record. Chem. Geol. 643.
Yao, L., Sun, C., Liang, Y., 2012. A parameterized model for REE distribution between low-ca pyroxene and basaltic melts with applications to REE partitioning in low-ca pyroxene along a mantle adiabat and during pyroxenite-derived melt and peridotite interaction. Contrib. Mineral. Petrol. 164 (2), 261–280.
Yin, A., 2000. Mode of Cenozoic east-west extension in Tibet suggesting a common origin of rifts in Asia during the Indo-Asian collision. J. Geophys. Res. Solid Earth 105 (B9), 21745–21759.
Zhang, L., 2014. Age and Petrogenesis of the Zedong Ophiolite, Southern Tibet. PhD thesis. Institute of Geology and Geophysics, Chinese Academy of Sciences, pp. 1–175. in Chinese with English abstract.
Zhang, L.-L., Liu, C.-Z., Wu, F.-Y., Ji, W.-Q., Wang, J.-G., 2014. Zedong terrane revisited: an intra-oceanic arc within Neo-Tethys or a part of the Asian active continental margin? J. Asian Earth Sci. 80, 34–55.
Zhang, C., Liu, C.Z., Wu, F.Y., Zhang, L.L., Ji, W.Q., 2016a. Geochemistry and geochronology of mafic rocks from the Luobusa ophiolite, South Tibet. Lithos 245, 93–108.
Zhang, L.-L., Liu, C.-Z., Wu, F.-Y., Zhang, C., Ji, W.-Q., Wang, J.-G., 2016b. Sr–Nd–Hf isotopes of the intrusive rocks in the cretaceous Xigaze ophiolite, southern Tibet: Constraints on its formation setting. Lithos 258-259, 133–148.
Zhang, C., Liu, C.-Z., Xu, Y., Ji, W.-B., Wang, J.-M., Wu, F.-Y., Liu, T., Zhang, Z.-Y., Zhang, W.-Q., 2019. Subduction re-initiation at dying ridge of Neo-Tethys: Insights from mafic and metamafic rocks in Lhaze ophiolitic mélange, Yarlung-Tsangbo Suture Zone. Earth Planet. Sci. Lett. 523, 115707.
Zhang, W.-Q., Dick, H.J.B., Liu, C.-Z., Lin, Y.-Z., Angeloni, L.M., 2021. MORB Melt Transport through Atlantis Bank Oceanic Batholith (SW Indian Ridge). J. Petrol. 62 (6).
Zhang, Z.-Y., Liu, C.-Z., Liang, Y., Zhang, C., Liu, T., Zhang, W.-Q., Ji, W.-B., 2022. Decoupled Trace Element and Isotope Compositions Recorded in Orthopyroxene and Clinopyroxene in Composite Pyroxenite Veins from the Xiugugabu Ophiolite (SW Tibet). J. Petrol. 63, 1–28.
Zhang, C., Liu, C.-Z., Bénard, A., Müntener, O., Ji, W.-B., Liu, T., Zhang, Z.-Y., Zhang, W.-Q., Wu, F.-Y., 2023a. Heterogeneous mantle beneath the Neo-Tethys Ocean revealed by ultramafic rocks from the Xiugugabu Ophiolite in the Yarlung-Tsangpo Suture Zone, southwestern Tibet. Contrib. Mineral. Petrol. 178 (8), 54.
Zhang, C., Liu, C.-Z., Liu, T., Ji, W.-B., Wu, F.-Y., 2023b. Generation of ultraslow-spreading oceanic crust traced by various mafic blocks from ophiolitic mélange in the Xigaze Ophiolites, southern Tibet. Contrib. Mineral. Petrol. 178 (8), 55.
Zhou, M., Robinson, P.T., Malpas, J., Edwards, S.J., Qi, L., 2005. REE and PGE Geochemical Constraints on the Formation of Dunites in the Luobusa Ophiolite, Southern Tibet. J. Petrol. 46 (3), 615–639, 625.
Zhou, B., Liu, J., Yan, J., Hou, C., Chen, X., Liu, C., Wu, F., 2023. Shearing-enhanced deep fluid circulation induces seismic anisotropy in the lower crust at slow-spreading oceanic ridges. Geology 51 (5), 465–470.